University of Texas at Arlington

MavMatrix

2023

MECHANICAL AND THERMAL PERFORMANCE OF ADDITIVELY MANUFACTURED DIGITAL MATERIALS

Layth Muayyad Ahmad

Recommended Citation

MECHANICAL AND THERMAL PERFORMANCE OF ADDITIVELY MANUFACTURED DIGITAL MATERIALS

By

LAYTH MUAYYAD AHMAD

Submitted in partial fulfillment of the requirements

for the degree of Master of Science in Mechanical Engineering at

The University of Texas at Arlington

May 2023

Arlington, Texas

Supervising Committee:

Dr. Ashfaq Adnan, Supervising Professor

Dr. Haiyang Huang

Dr. Robert Taylor

DEDICATION

I dedicate this work to those who have been with me during this journey, and I am deeply appreciative of the support, guidance, and encouragement I have received from them. As I look back on the years that led me to this point, I am reminded of countless memories, both joyful and challenging, that have shaped my experiences and the person I have become. I would like to thank my supervisor, Dr. Ashfaq Adnan, whose unwavering support, mentorship, and inspiration have been invaluable. His passion for research and commitment to making a positive impact on the world have allowed me to be part of something much more significant than myself. I am also grateful to my colleagues and lab mates in MMPL for making this experience both enriching and enjoyable.

My deepest gratefulness goes to my family, who have provided constant love and support as the foundation of my achievements. To my father, Dr. Muayyad, my role model and source of inspiration; my mother, Huda, whose love and nurturing have guided me every step of the way. To my brothers, Huthaifa, Muath, and Abdelrahman, who have always encouraged and motivated me to pursue my dreams. Your unwavering support has been the cornerstone of my success, and I could not have achieved this without you. To my friends, thank you for your friendship and for making my life a wonderful journey. And to Mustafa, who may not be able to read this, I hope I have made you proud.

Finally, I dedicate this thesis to Allah the Almighty, the most merciful and compassionate. I am grateful for the strength and guidance, and the power of mind that Allah has provided me throughout my academic journey. "And your Lord is going to give you, and you will be satisfied (93:5)"

ABSTRACT

MECHANICAL AND THERMAL
PERFORMANCE OF ADDITIVELY
MANUFACTURED DIGITAL MATERIALS

Layth Muayyad Ahmad M.S

The University of Texas at Arlington, 2023

Supervising Professor: Ashfaq Adnan

Over the past decades, additive manufacturing has become a critical material processing tool. All ranges of materials including polymers, composites, metals, and ceramics can be used to fabricate structures with complex geometries that are nearly impossible to build using conventional fabrication process. Recently, additive manufacturing methods to build polymeric structures have been advanced significantly. In particular, the emergence of multi-material printers has made it possible to seamlessly print hybrid and digital materials where materials components and compositions are digitally varied to construct fully tailored material system. In this work, using a commercially available polyjet printer (Stratasys J850 Prime 3D printer), digital materials with varying concentrations of viscoelastic Agilus30 and Vero plastic materials are created. Digital and hybrid materials with varied Shore A hardness values of 30, 60, and 95 are produced by mixing Agilus30 Black with VeroMagentaV. Then their mechanical and thermal damage behavior was studied. Dog-bone and rectangular specimens are used for tensile testing at different strain rates,

with the latter having an elliptical defect in the center. Due to its higher stiffness and fracture stress, the hybrid material SH95 material behaves plastically, while the hybrid material SH30 and hybrid material SH60 materials respond similarly and are characterized by elongation and flexibility. Testing the materials' capacity to absorb dynamic energy using drop tower impacts reveals a nonlinear link between material composition and acceleration decrease. Additionally, Agilus30 Black is subjected to laser heating studies to examine its thermal damage characteristics and behavior when exposed to heat, providing insights into heat transmission and thermal stability characteristics. This study contributes valuable knowledge to the properties and performance of hybrid materials, paving the way for future research in material selection and optimization.

TABLE OF CONTENTS

LIST OF FIGURES

viii

LIST OF TABLES

CHAPTER ONE

INTRODUCTION

With recent advances in additive manufacturing, specifically Polyjet 3D printing, the investigation of the mechanical properties of hybrid materials has drawn significant attention to the additive manufacturing community. In principle, additive manufacturing of hybrid materials means fabrication of a structure using multiple materials at the same time. The conventional single material 3D printing methods such as stereolithography (SLA), selective laser sintering (SLS), and Fused Deposition Modeling (FDM) [3-5, 16] have limited capabilities to print fully blended and tailorable hybrid materials. Recently, polyjet printers have been introduced where multiple liquid polymer resins can be fed to deposit materials in blended or layer-by-layer manner, Figure 1. The advantage of using Polyjet 3D printing is the ability to produce high-quality multi-material parts with high accuracy and surface finish. Additionally, such printers typically allow a large build volume, enabling the creation of sizable and complex components. Furthermore, this technique is compatible with a wide variety of materials, from flexible elastomers to rigid polymers, enabling the easy production of complex, multi-material prototypes [24]. Potential applications of such hybrid structures include dynamically similar biomaterials, protective equipment, and energy absorbing structures [1-2, 11-15].
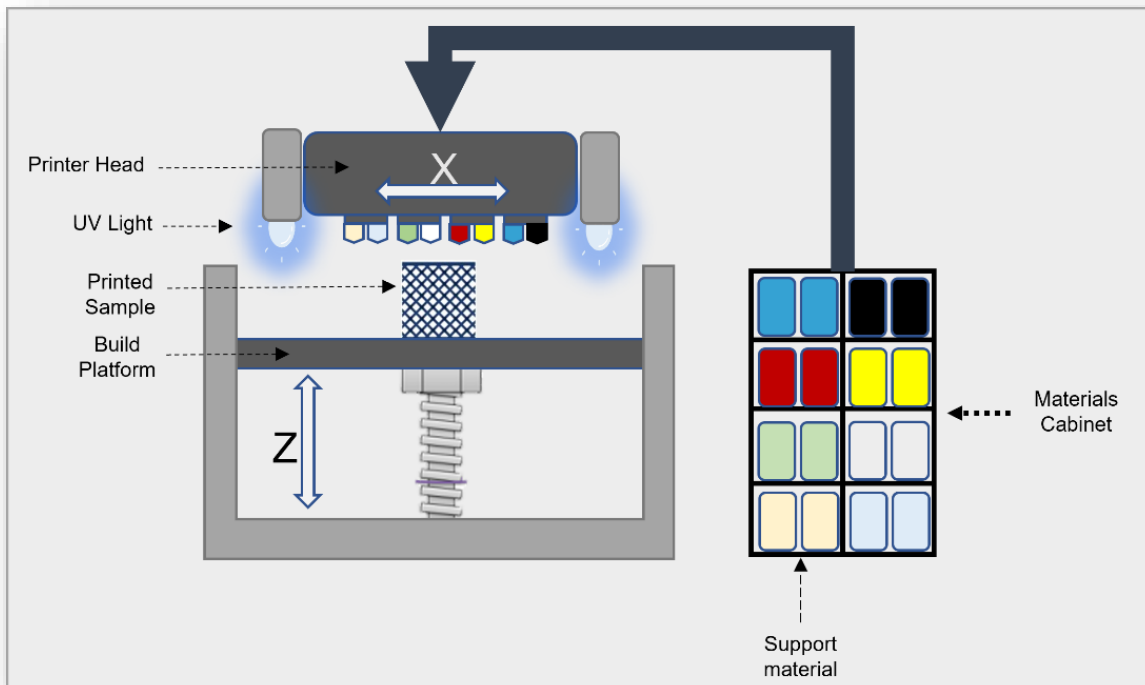
Figure 1: Illustration of the PolyJet 3D printing process.

For energy absorption characterization, traditionally static or dynamic mechanical tests are performed. For static test, a sample is subjected to a static impact test and its stress-strain response until failure is observed. The area under the stress-strain curve is typically considered as a measure for energy absorption. For nonlinear materials such as polymers or elastomers, it is also important to know their static tensile failure and damage mechanisms. For dynamic mechanical tests, there are many methods available including drop impact, split Hopkinson bar, high-speed ballistics tests etc. In principle, all these methods track the kinetic energies of a moving impactor before and after an impact, the difference in kinetic energies is taken as a measure for energy absorption.

The majority of material mechanical performance testing reported in the literature are conducted using a static load test. This is in large part due to the simplicity of the testing procedure. Such a test is also adequate to design materials for many applications However, there are also numerous

applications for hybrid 3D printed materials under dynamic loading. In particular, 3D printed materials are being investigated for the use as protective equipment to enhance energy absorption. A material that performs well under static loading does not necessarily perform well under dynamic loads [11]. The presence of kinetic energy and wave propagation make the analysis much more complex and thus different measurement and analysis methods must be employed. Most mechanical testing studies are performed on single material specimens with or without defects [6-7]. A few studies investigate the mechanical properties of hybrid materials with varying concentration of material constituents [8-9, 18, 25]. This research explores the potential of creating hybrid materials by combining two distinct materials with varying characteristics. The resulting materials demonstrate a range of stiffness, both with and without intentionally introduced defects. Additionally, the study investigates the performance of these novel hybrid materials when subjected to dynamic loads.

In this study, we utilize a Stratasys J850 Prime multi-material 3D printer which allows us to print variable concentrations of viscoelastic Agilus30 and Vero plastic materials. We have analyzed the mechanical response of varying concentration viscoelastic Agilus30 Black and VeroMagentaV plastic under static tensile tests and dynamic impact drop tower tests. For both load cases we investigate specimens of 30, 60, and 95 shore A hardness. In the static test specimens, an elliptical shaped defect is introduced for comparison to samples without defects. Cube shaped specimens are used in the drop tower impact tests. An indication of the amount of energy absorbed is measured by recording the difference in acceleration from the top surface of the impacted cube to the base of the cube; such a measurement is a direct indicator of the change in kinetic energy across the material system [11].

Directed energy sources, such as lasers, are also becoming increasingly prominent in various industries and applications. Understanding the thermal properties and behavior of materials under laser irradiation is essential for material selection, engineering applications, and the development of protective measures. However, research on the thermal performance of 3D printed digital materials under directed energy sources remains limited [32, 33-37].

This study has a dual objective: (1) to analyze the mechanical response of varying concentration viscoelastic Agilus30 Black and VeroMagentaV plastic under static tensile tests and dynamic impact drop tower tests, evaluating their performance under different loading conditions as mentioned above, and (2) to examine the thermal properties and efficacy of two digital materials that have been 3D printed, Agilus30 Black and Digital ABS, under the effect of laser irradiation. The study involves a variety of sample thicknesses, ranging from 0.25 mm to 6 mm, to evaluate the correlation between material thickness and thermal performance. A fiber-coupled continuous wave (CW) laser with a power output of 250 mW is utilized to supply the necessary thermal energy.

This comprehensive investigation will contribute to a deeper understanding of hybrid materials' mechanical and thermal properties, behavior under various loading conditions, and performance under directed energy sources. The findings hold promise for future research, material selection, and engineering applications, particularly where directed energy is a critical factor. By exploring the potential of these hybrid materials, researchers and engineers can optimize their designs and develop innovative solutions across numerous engineering disciplines.

CHAPTER TWO

MECHANICAL PERFORMANCE OF DIGITAL MATERIALS

The strength, functionality, and durability of the resulting objects are significantly affected by the mechanical properties of the digital materials used in 3D printing. For these materials to be used most effectively across a range of industries, it is important to understand how they behave to different mechanical stresses [14–15]. As a result, for informed material selection and design optimization, a thorough understanding of the mechanical behavior of digital materials, including tensile and compressive properties, is required.

The structure of this chapter is as follows: The experimental setup is described in Section 2.1, "Methodology," and includes the 3D printer, materials and sample preparation, specimen design, and experimental work setup. Results from the drop tower impact test and tensile testing are analyzed in Section 2.2, "Results and Discussion," which also discusses the mechanical behavior of the digital materials under various situations.

2.1 Methodology

2.1.1 3D printer

The J850 Prime is an advanced 3D printer known for its versatility in producing multi-color and multi-material parts through a single printing process. This printer can achieve layer resolutions as fine as 14 microns and has a build volume of up to 490 x 390 x 200 mm (19.3 x 15.35 x 7.9 in.). Unique to PolyJet 3D printers, multiple materials can be combined within a single layer, resulting

in a gradient of properties in the finished object. For example, flexible and rigid sections can coexist within one layer, enabling the creation of complex structures with diverse applications. This sets PolyJet apart from other 3D printing methods and opens up new design and production possibilities. Moreover, the J850 Prime supports a broad array of model materials, including the Vero™ family with neutral shades and vivid VeroVivid™ colors, the flexible Agilus30™ family, transparent VeroClear™ and VeroUltraClear, and VeroUltra™ opaque materials in black and white. This allows the printer to accommodate a wide range of digital model materials with over 500,000 colors. Additionally, Digital ABS Plus™ and Digital ABS Plus™ are available in ivory and green, providing an improved version of the widely used ABS in FDM printers with heat resistance. The printer uses soluble SUP706B™ as the support material. The J850 Prime also features four build modes with varying combinations of resins and resolutions [23].

To streamline the printing process, the printer utilizes GrabCAD Print™ software, which enables direct printing from popular design software and supports various file formats, including 3MF, STL, OBJ/VRML, STEP, and native CAD formats. This software also provides detailed previews of the model, allowing for adjustments before printing.

2.1.2 Materials and sample preparation

In this work Agilus30 Black and VeroMagentaV are the two materials used to make specimens. GrabCAD gives the user the choice to combine materials together to print specimens with different stiffness and shore A hardness. In this work, 4 material combinations were selected for testing. Table 1 summarizes the specimens used in this study for tensile and dynamic impact testing where all the samples are designed using SOLIDWORKS software. The first set of specimens were fabricated using only Agilus30 Black and the fourth set made from VeroMagentaV which was

considered just for the drop tower experiment. The second and the third sets were fabricated by mixing Agilus30 Black and VeroMagentaV at certain percentages, but the majority was Agilus30. While using Digital Material mode in GrabCAD, one of five modes you can use based on the materials, the printed sample's color, the use of it, etc., it allows you to pick any materials you want to mix in order to print a hybrid sample from the two or the three materials family – Vero, Agilus30, and Digital ABS – you have picked. When mixing Agilus30 Black and VeroMagentaV, which is what was selected in this case, the software provides several choices that have predefined values for the shore A hardness ranging from 40 and 95. For this experiment, Shore A hardness of 60 and 95 were selected for the second and the third set of specimens respectively.

Table 1: The hybrid materials specimens used in tensile and impact tests.

	Agilus30 Black [SH 30]	Hybrid material with shore A hardness 60 [SH 60]	Hybrid material with shore A hardness 95 [SH 95]	VeroMagentaV
Shore A hardness	30	60	95	-
Tensile test 1 specimen design				-
Acronyms	SH30	SH60	SH95	-
Tensile test 2 specimen design				-
Acronyms	SH30-Rec	SH60-Rec	SH95-Rec	-
Impact test specimens (drop tower) design				
Acronyms	SH30-Cube	SH60-Cube	SH95-Cube	Vero-Cube
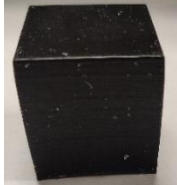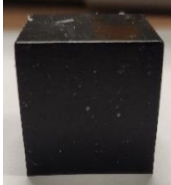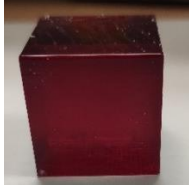
A group of scientists from the RMIT university studied how different printing angles could affect the mechanical properties of the materials using Stratasys J750 3D printer [8]. They found out that

the tensile test results of the specimens printed with angle of 45 were 10% weaker compared to the ones printed in parallel to the printer head [19]. Accordingly, to study the behavior of the materials over the hardness' spectrum in this study. All the specimens were printed in the positive direction of X axis, which is the default direction of the printer's head.

As mentioned earlier, Stratasys J850 Prime uses SUP706B™ as a support material which is soluble in the water. GrabCAD gives the user the chance to choose between two modes of support, glossy or matte. Usually, the mode will be chosen based on the geometry, the material in use, and the surface finish quality desired of fabricated part. Glossy in general uses less support and it will be deposited on the bottom half of the part with good surface finish quality, also improves the specimen's stiffness [20]. On the other hand, using matte will use more support materials because it will cover the entire part with support, and the surface finish quality will be much less desired compared to the glossy finish, and it might need post-processing such as polishing in some cases. All fabricated specimens for this work were printed in glossy mode.

Moreover, the relationship between Agilus30 content and total mass of SH30, SH60, and SH95 materials was investigated using cube-shaped specimens with edge lengths ranging from 1 to 5 inches. Estimations were obtained using GrabCAD software. A non-linear trend was observed in the Agilus30 percentage to total mass ratio for all materials. SH30 and SH60 showed comparable percentages, while SH95 showed a consistently lower percentage of Agilus30 to the total mass, which could contribute to its higher stiffness. These observations highlight that the proportion of Agilus30 in the sample mass behave non-linearly across different cube sizes and materials, and understanding this non-linear relationship could help optimize material composition for various applications (Appendix Tables 4-6)

2.1.3 Specimens Design

The specimens for the first tensile test were designed following the ASTM D-638 standard Type IV for SH30, SH60, and SH95 since these materials have a behavior of rubber-like materials [9, 21].

Figure 2 (A) shows the design and the dimensions of the hybrid specimens, the proposed mixed combination was in the test section (65 mm), but the ends were made of different Vero materials and colors in order to avoid any elongation in the grip's region since all the hybrid materials act more like a rubber as previously mentioned. The overall length is 115 mm, the width of the ends is 19 mm, and 6 mm in width of the narrow section. The thickness of the specimen is 3.6 mm.

For the second tensile test specimens, all three specimens' shapes were designed similarly, Figure 2 (B). Rectangular shape with 152.4 mm in length, 25.4 mm in width, and 3.6 mm in thickness. Moreover, a defect with an ellipse shape with width of a = 5 mm and height of b = 0.1 mm was made in the center of the sample that goes through the entire thickness. The goal is to understand how the hybrid materials with different shore A harnesses would deform compared to the flawless specimens. The fabrication of this batch of specimens were similar to the one before in the sense of the material used to made them, where the test section (101.6 mm) is made of the mixed materials for SH30, SH60, and SH95 but the ends were made from Vero materials and colors to avoid any elongation in the grip's region while running the test.
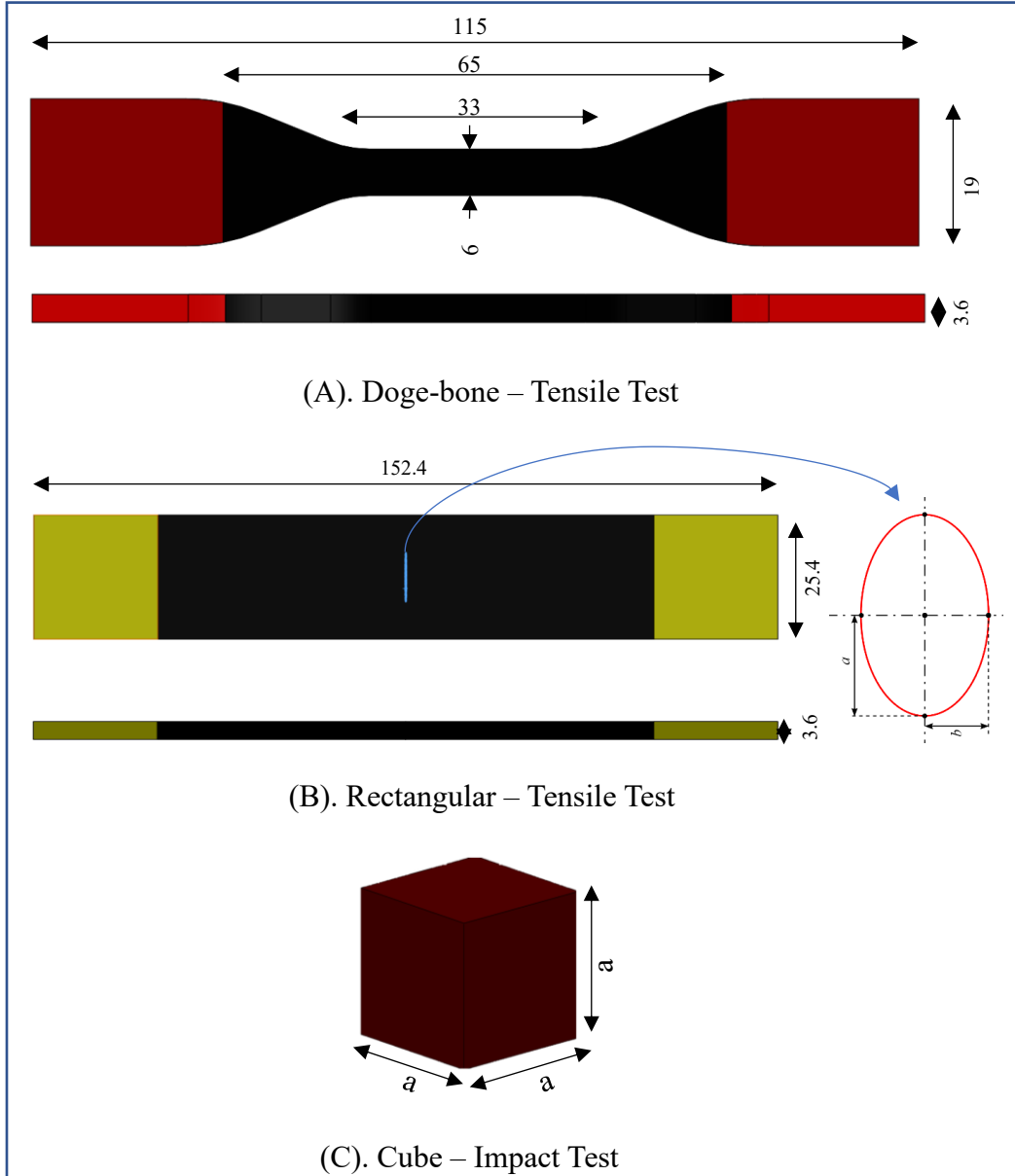
Figure 2: Testing specimens. (A) The dimensions in mm of the first tensile testing specimen designed based on ASTM standard D 638 type IV with minor changes [9]. (B) The dimensions in mm of the second tensile testing specimen. The dimensions of the ellipse a = 5 mm, b = 0.1 mm. (C) The dimensions in mm of the drop tower test specimen. The dimension of the edge a = 25.4 mm

The third and the last set of specimens took the shape of cube, Figure 2 (C). These samples were made for a dynamic impact test at low speed using drop tower which will be discussed further later in this work. All the specimens were exactly similar in terms of design and dimensions. A cube with an edge length of 1 in (25.4 mm) was fabricated. The materials had the same mix combination from the tensile test; SH30, SH60, Sh95, and Vero.

2.1.4 Experimental Work Setup

2.1.4.1 Tensile Test

Shimadzu's AGS-X series universal / tensile testing machine with load cell of 5 KN was used to perform the mechanical tensile tests with different strain rates. These rates were selected in order to run the tensile testing within a fracture time between 30 seconds and 5 minutes as ASTM D-638 standard suggests. Both specimens' shapes for tensile test (Dog-Bone and Rectangular) were tested at the same strain rate for each proposed material.

Three specimens at least were tested for each material we studied. The specimens of Agilus30 Black and hybrid material SH60 were both tested under stroke rate of 18 and 25 mm/min as most of the tested section made of viscoelastic material which allow these specimens to have a high deformation. On the other hand, the hybrid material SH95 was only tested under stroke rate of 18 mm/min since SH95 is stiffer and would deform less and break faster. The results from the testing machine can be accessed using the TRAPEZIUM X software, where the results can be exported in different forms to apply any post-process afterward. The setup also includes a Photron FASTCAM NOVA S9 high speed camera to capture the specimen's facture as it will be presented later in this work, Figure 3 .

22
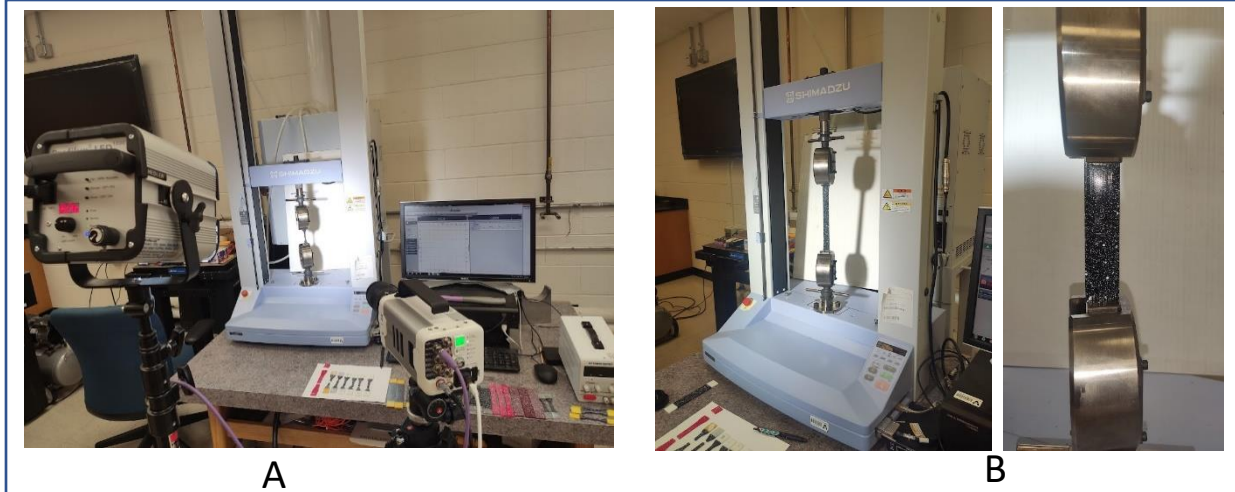
Figure 3: A. Tensile testing setup. B. Universal testing machine including the tensile testing fixture.

2.1.4.2 Impact test

The dynamic impact test was done by using a drop tower that was constructed inside the lab. It followed the same setup that was used to run another experiment in the lab to study different lattice structures [11]. The drop tower's framework is built of wood. The interior of the vertical columns is attached with low friction rails that enable the impact mass to move easily up and down. The top of the impacting mass is mounted with a steel plate that has an electromagnet linked to it. A mechanical winch is used to hoist a rope that has an electromagnet fixed to it. LabVIEW manages the electromagnet release, enabling a controlled drop that coincides with the beginning of data collection. Each cube is prepared by placing it in the impact region. The purpose of the drop tower tests is to estimate the energy absorption of the different materials under dynamic loading. In a static load case, the presence of inertia is negligible and thus the energy absorbed is purely a function of force and deformation. However, dynamic energy absorption is generally quantified by the difference in kinetic energy a material system experiences under external loading. The kinetic energy change of the material can be understood by equation (1).

$$\Delta K = \frac{1}{2} m \left(\int_{t_1}^{t_2} \ddot{x}_T(t)\, dt - \int_{t_1+\Delta t}^{t_2+\Delta t} \ddot{x}_B(t)\, dt \right)^2 \qquad (1)$$

Equation (1) shows that the change in kinetic energy is directly related to the change in acceleration across the material. In the drop tower impact experiments an accelerometer is positioned on a steel plate that is placed on the top of the test specimen. A second bottom plate is attached to the base of the drop tower where the test specimen is positioned. The mechanical wave propagation of due to the impact takes time to travel through the specimen. Therefore, when measuring the acceleration felt by the bottom of the structure, there is a time delay Δt that is dictated by the material stiffness and density. The positioning of the accelerometer to measure the reduction in acceleration across the cube. The cube specimen is placed as close to the center of the impact plate as possible to ensure the impact is in the center of the test specimen. A schematic of the drop tower system, data acquisition, and high-speed videography, as well as the variables described in equation (1) are shown in Figure 4.
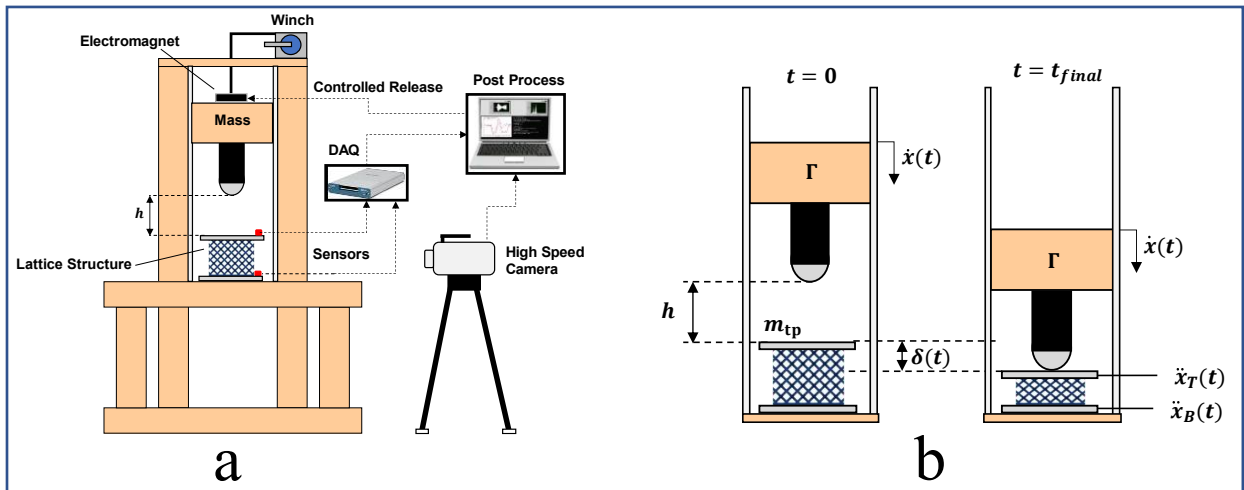
Figure 4: a. Schematic of drop tower experiment with sensors, data acquisition, high speed camera, electromagnetic release mechanism, and data post processing. b. Schematic of the drop

tower impact with variables Γ (impactor mass), m (specimen mass), h (drop height), δ (specimen deformation), $\dot{x}$ (impactor velocity), $\ddot{x}_T$ (specimen top acceleration), and $\ddot{x}_B$ (specimen bottom acceleration)

2.2 Results and Discussion

2.2.1 Tensile Testing

2.2.1.1 Agilus30 Black (SH30 & SH30-Rec)

The stress-strain curves of seven Agilus30 Black (SH30) specimens that were obtained from tensile testing at 25 mm/min strain rate are illustrated in Figure 5. The SH30 dog-bone specimens showed a strain of approximately 2.5 times their initial length.

In the second part of the experiment, the mechanical properties of SH30 Rectangular specimens with a centrally located elliptical defect extending throughout the entire specimen's thickness were evaluated also at 25 mm/min strain rate. Each of the three specimens fractured in a unique area, except for the first specimen, which fractured in the middle. This specimen also broke the quickest, but its stress-strain curve closely resembled that of the second specimen. These observations are visible in the stress-strain curves shown in Figure 5.

The differences in fracture behavior among the SH30 Rectangular specimens can be related to the chemical characteristics of the material and the small size of the elliptical defect. The adhesive

nature of the material, together with the small size of the defect, may have contributed to the seemingly flawless functioning of some specimens. This emphasizes the sophisticated relationship between Agilus30 Black sample material parameters, defect characteristics, and mechanical behavior.
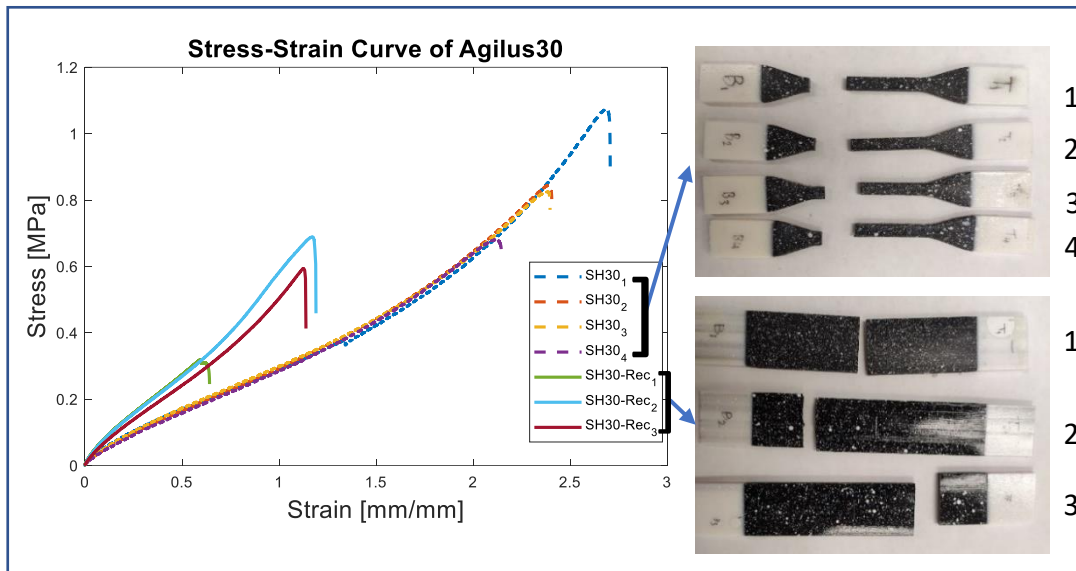
Figure 5: The Stress-Strain curves of the Agilus30 specimens obtained after tensile testing, including 4 dog-bone specimens, and 3 rectangular specimens with elliptical defect in the middle.

In a subsequent round of tensile testing, a new set of specimens were tested at an 18 mm/min strain rate to obtain similar data for all three materials in this study. Figure 6 displays the stress-strain curves for six dog-bone specimens, with three tested at an 18 mm/min strain rate and the remaining three at 25 mm/min from the test before. All the curves followed a similar trend, and the overall results were found to be comparable between the two strain rates.
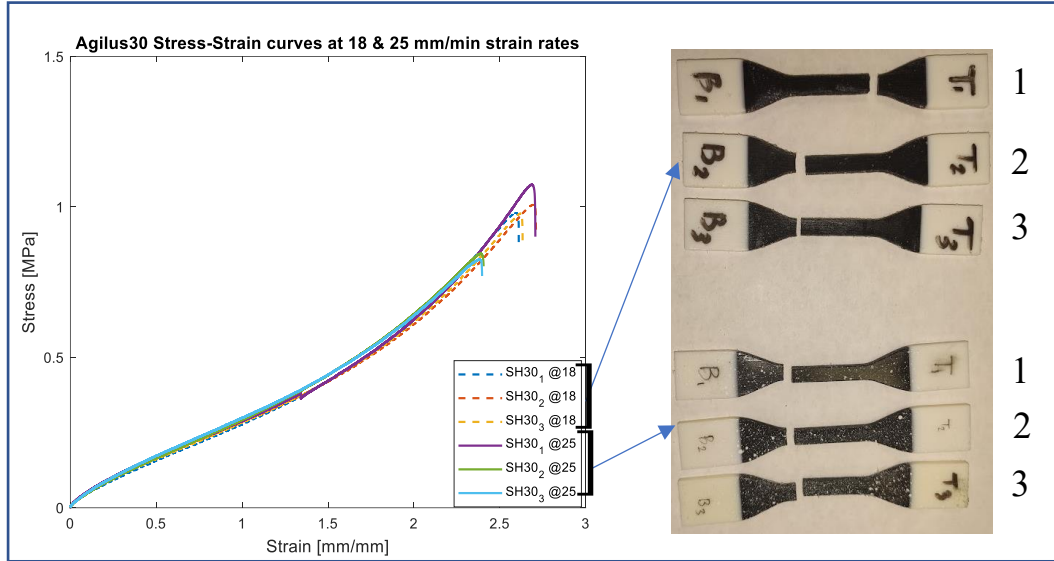
Figure 6: The Stress-Strain curves resulting from the tensile testing of 6 dog-bone shaped Agilus30 specimens. Three of the specimens were subjected to a strain rate of 18 mm/min, while the remaining three were tested at 25 mm/min.

In addition to the dog-bone specimens, rectangular specimens with defects were also subjected to tensile testing at 18 mm/min strain rate to further investigate the mechanical properties of the three materials. The stress-strain curves for these rectangular specimens that broke in the middle exhibited similar trends as well and can be seen in Figure 7, highlighting the consistency in material behavior across different sample geometries and strain rates.
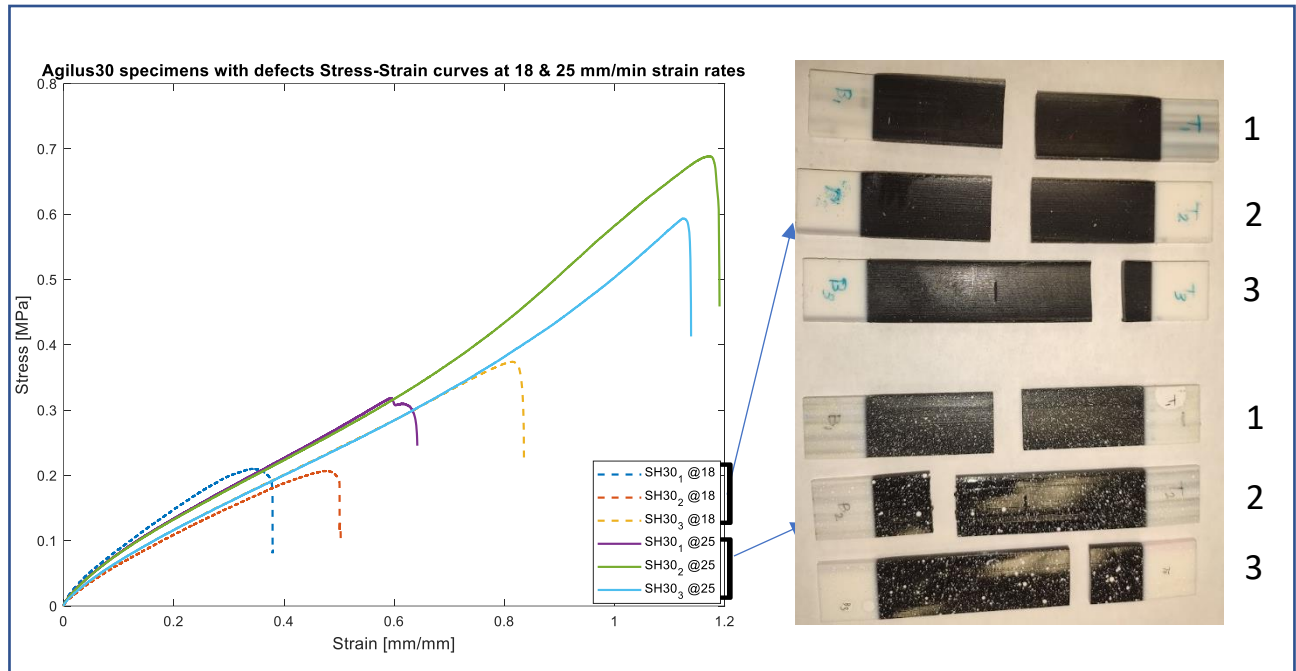
Figure 7: The Stress-Strain curves obtained from the tensile testing of 6 rectangular Agilus30 specimens, each containing an ellipse-shaped defect at the center. Three specimens were tested at a strain rate of 18 mm/min, while the remaining three were tested at 25 mm/min.

2.2.1.2 Hybrid Material (SH60 & SH60-Rec)

Figure 8 presents the stress-strain curves for the hybrid material SH60 dog-bone specimens and SH60 rectangular specimens at 25 mm/min. The stress-strain curves for the whole set of SH60 specimens show identical patterns, indicating that the material displayed equivalent mechanical behavior throughout the testing procedure. The SH60 rectangular specimens, on the other hand, yielded unexpected results, with the second and third specimens fracturing in the center and the first specimen breaking in a peculiar spot. This observation underlines the possible impact of

specimen geometry and the presence of flaws on the hybrid material's overall mechanical characteristics and fracture behavior.

The consistent behavior of the SH60 dog-bone specimens' curves implies a uniform performance of the hybrid material, which is important in understanding its suitability for different uses. Furthermore, the fracture locations observed in the SH60 rectangular specimens indicate that the presence of defects or specific geometric features may have a substantial influence on the mechanical response and eventual fracture of a material.

Figure 8: The Stress-Strain curves of the hybrid material SH60 specimens obtained after tensile testing, including 4 dog-bone specimens, and 3 rectangular specimens with defect of ellipse shape in the middle.
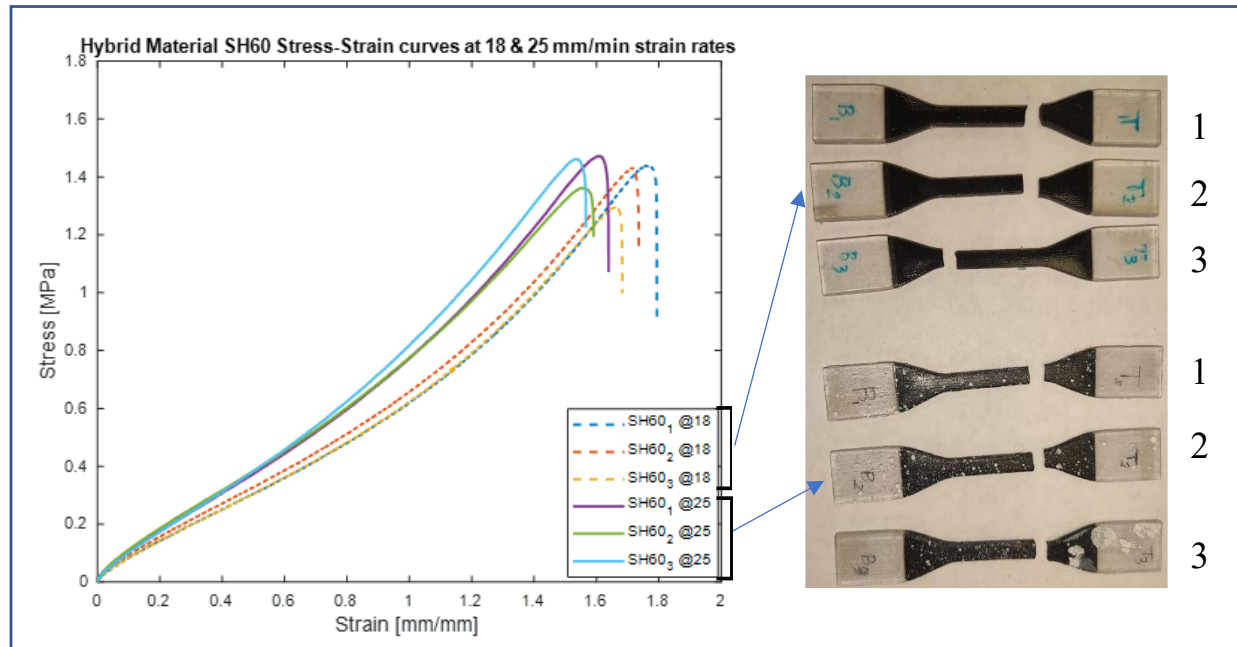
Figure 9: The Stress-Strain curves resulting from the tensile testing of 6 dog-bone shaped hybrid material SH60 specimens. Three of the specimens were subjected to a strain rate of 18 mm/min, while the remaining three were tested at 25 mm/min.

In addition, the mechanical properties of the hybrid material SH60 were thoroughly examined at 18 mm/min strain rate using both dog-bone shaped and rectangular specimens, as illustrated in Figure 9 and Figure 10. As Figure 9 presents, the stress-strain curves for these dog-bone specimens followed similar patterns, with those tested at 18 mm/min showing slightly higher elongation compared to those tested at 25 mm/min. This observation implies that the mechanical properties of SH60 material, specifically in terms of elongation, are slightly influenced by the strain rate.
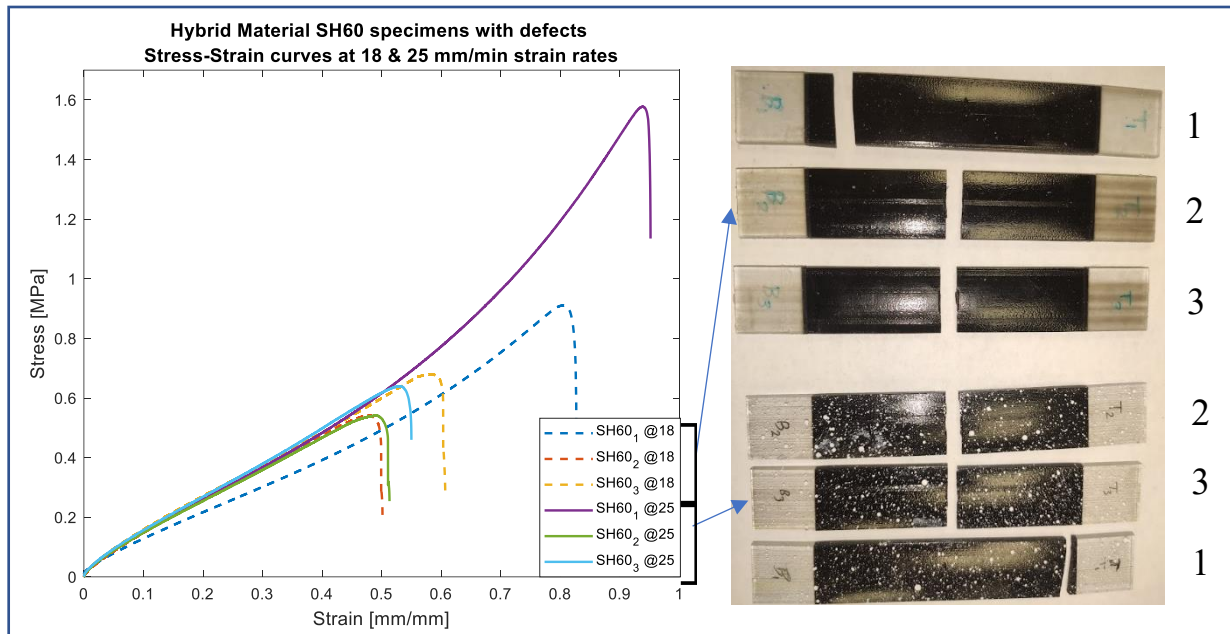
Figure 10: The Stress-Strain curves obtained from the tensile testing of 6 rectangular hybrid material SH60 specimens, each containing an ellipse-shaped defect at the center. Three specimens were tested at a strain rate of 18 mm/min, while the remaining three were tested at 25 mm/min.

The results of tensile testing for rectangular SH60 specimens, which included an ellipse-shaped defect in the center, are presented in Figure 10. The tests were conducted at two different strain rates, 18 mm/min and 25 mm/min. The stress-strain curves obtained from the tests exhibited similar patterns for specimens that fractured at the midpoint. This suggests that, although the existence of an imperfection in the specimen, the mechanical performance of the SH60 substance remained uniform with that of the dog-bone specimens. Furthermore, it was observed that the strain rate exhibited a negligible influence on the material's mechanical behavior, causing only a slight variation in its elongation.

2.2.1.3 Hybrid Material (SH95 & SH95-Rec)

The stress-strain curves for the SH95 hybrid material specimens and the SH95-Rec specimens with a centrally positioned elliptical flaw can be seen in Figure 11. As proposed it was observed that the SH95 samples displayed a reduced strain and increased stress in comparison to the SH30 and SH60 samples, due to their higher Shore A hardness value of 95. The increased level of rigidity led to a material behavior that resembled that of plastic, as opposed to the materials that were previously examined, which exhibited greater flexibility. The SH95 specimens, which were rectangular in shape, exhibited an identifiable fracture behavior as they all fractured at the elliptical defect. The observed regularity in the material's behavior indicates a significant impact of its increased rigidity on its mechanical properties, particularly when flaws are present, leading to more predicted fracture configurations.
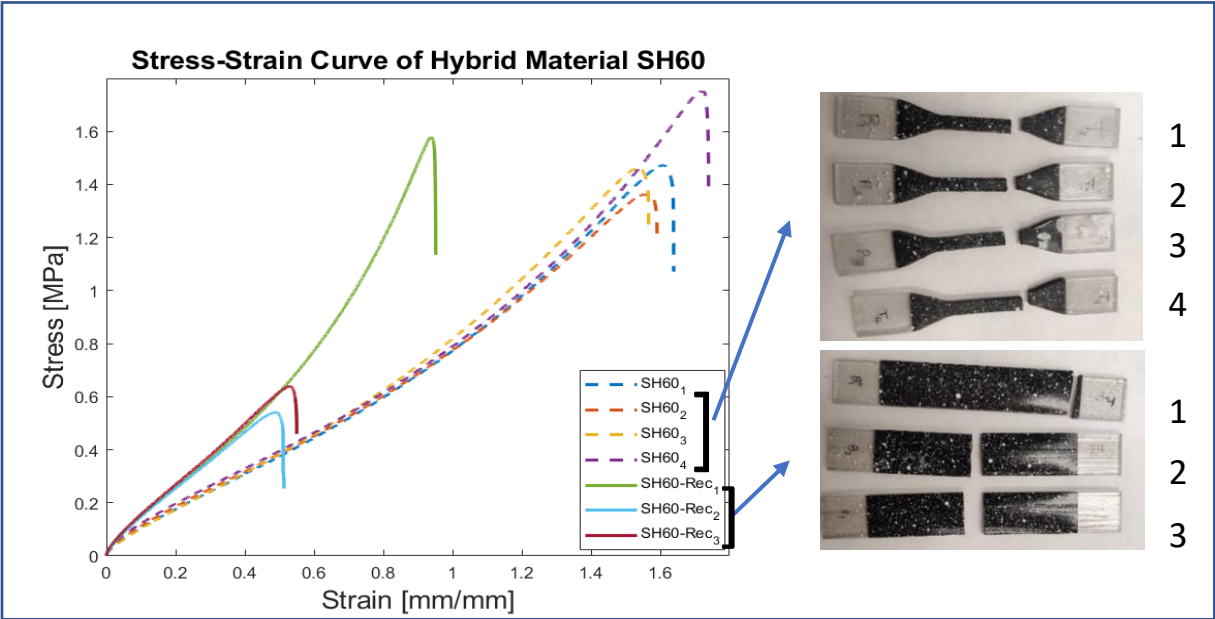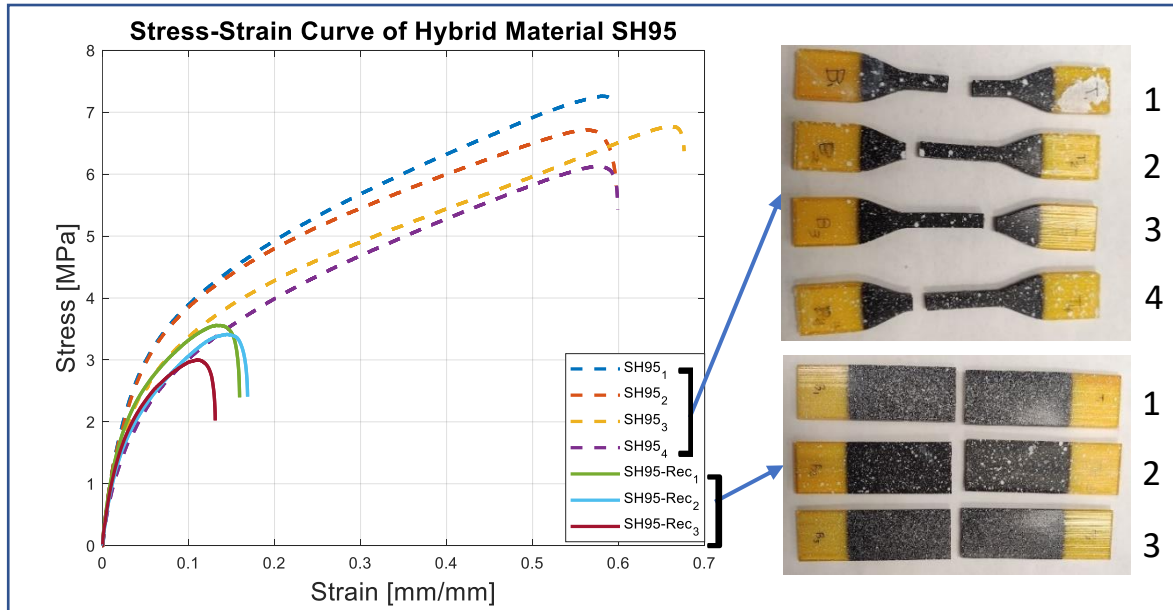

Figure 11: The Stress-Strain curves of the hybrid material SH95 specimens obtained after tensile testing, including 4 dog-bone specimens, and 3 rectangular specimens with defect of ellipse shape in the middle.

Figure 12 (A) presents a comparison of the stress-strain curves of Agilus30 SH30 and hybrid material SH60 at strain rates of 18 and 25 mm/min for both dog-bone and rectangular specimens. The comparison shows that, despite differences in strain rates and specimen shapes, the materials exhibit comparable mechanical behavior, with the SH60 material showing slightly higher stress at lower strain levels, indicating a stiffer response to deformation.

The mechanical responses of the SH30 and SH60 materials appear to be similar, as observed in Figure 12 (B). However, the SH95 material displays different properties due to its increased stiffness and greater fracture stress. The SH30 material, which has the highest elasticity of the three, is characterized by its ability to stretch significantly before breaking. This characteristic is attributed to the material's softer Shore A hardness, which makes it more flexible and compliant. The stress-strain curve of the SH30 material shows a gradual increase in stress as strain increases, emphasizing the resilience and adaptability of this material.
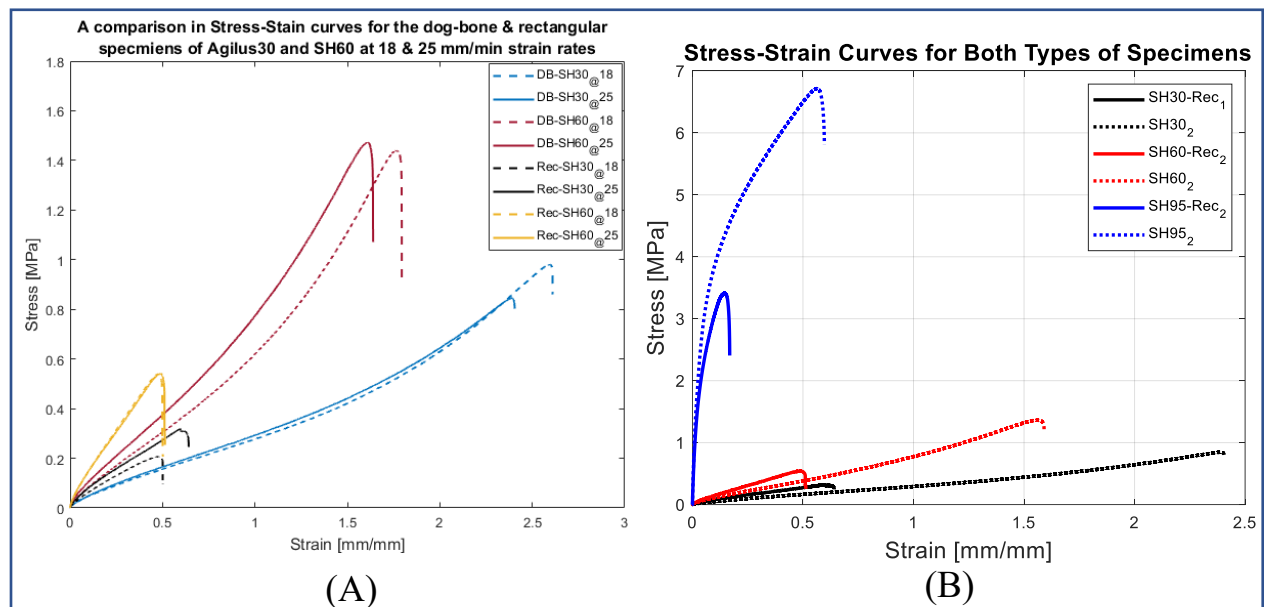
Figure 12: (A). A comparison in stress-strain curves of Agilus30 SH30 and hybrid material SH60 at 18 and 25 mm/min strain rates for dog-bone and rectangular specimens' shapes. (B). A comparison in stress-strain curves of Agilus30 SH30, hybrid material SH60, and hybrid material SH95 for dog-bone and rectangular specimens' shapes.

The SH60 material exhibits mechanical properties that fall within the range of those observed for the SH30 and SH95 materials. Despite having lower elasticity compared to SH30 material, SH60 demonstrates a significant degree of flexibility and elongation. The stress-strain behavior of the SH60 material exhibits a resemblance to that of the SH30 material, yet with higher stress values at lower strain levels, signifying a comparatively rigid reaction to deformation.

The SH95 material, with its higher Shore A hardness, is characterized by increased rigidity and fracture stress. The stress-strain curve clearly demonstrates a lower strain and a higher stress at the point of failure, signifying the more plastic-like nature of the material. The distinct mechanical response of the SH95 material is due to the increased cross-linking within the polymer network, which results in a denser and more rigid structure. The molecular structure and chemical composition of these materials can also significantly influence their perceived mechanical capabilities. The variations in Shore A hardness values are likely attributable to different proportions of monomers, cross-linking agents, and the UV intensity that these materials received from the head printer during the fabrication process. A comprehensive examination of the chemical and structural differences between these materials could shed light on the underlying causes of their distinct mechanical behavior.

Table 2: Undeformed, Initial Deformation, and Right before complete fracture of each rectangular specimen with ellipse in the middle during the tensile testing at 25 mm/min strain rate taken with high-speed camera.

	Undeformed	Initial Deformation	Right before complete fracture
SH30-Rec			
SH60-Rec			
SH95-Rec			

2.2.2 Drop Tower Impact Tests

Drop tower impact tests were conducted for the four different cube shaped materials as described in Table 1. An indication of the dynamic energy absorption is recorded by the acceleration difference across the top impacted plate and the base of the structure as seen in Table 3. Three tests were conducted for the SH30, SH60, and SH 95 materials, and two tests were conducted for Vero. Each drop tower test was conducted with a constant impact mass of 5.53 kg and 2 m/s. The average acceleration reduction across the material specimens is 641, 562, 677, and 721 g's for the SH30, SH60, SH95, and Vero, respectively. In our experiments, we utilize acceleration reduction across the material system as an indication of the energy absorbed by the structure. The results indicate that acceleration reduction is similar for the SH30 and SH95, lower for the SH60, and highest for the Vero. The SH30, SH60, and Sh95 materials all contain a different concentration of Agilus30 Black, a well-known viscoelastic velocity dependent material. The materials containing variable concentration of Agilus30 display a nonlinear acceleration reduction with increasing Agilus30 Black percentage.

Table 3: The acceleration measured by the accelerometers on the top plate, the bottom plate and the different between them.

	Top Plate Acceleration [g's]	Bottom Plate Acceleration [g's]	Reduction in Acceleration [g's]
SH30_1	-1005	-331	674
SH30_2	-938	-336	602
SH30_3	-948	-301	647
SH60_1	-869	-339	530
SH60_2	-882	-321	561
SH60_3	-942	-346	594
SH95_1	-1019	-382	637
SH95_2	-984	-321	663
SH95_3	-1054	-324	730
Vero_1	-1040	-343	697
Vero_2	-1052	-306	746

Additionally, the total impulse or momentum change of the impact event is a clear indicator of the performance of a dynamically loaded material. In terms of energy absorption, the longer time a load can be dissipated over indicates a "more protective" material. We observed that the time in which the impact phase of the impact event happened over got larger with the increasing concentration of Agilus30. Thus, it was seen that the stiffer materials had a smaller momentum change and the less stiff materials, those with higher concentration of Agilus30, had a larger momentum change. Momentum is proportional to kinetic energy, and thus higher momentum change should yield higher energy change.
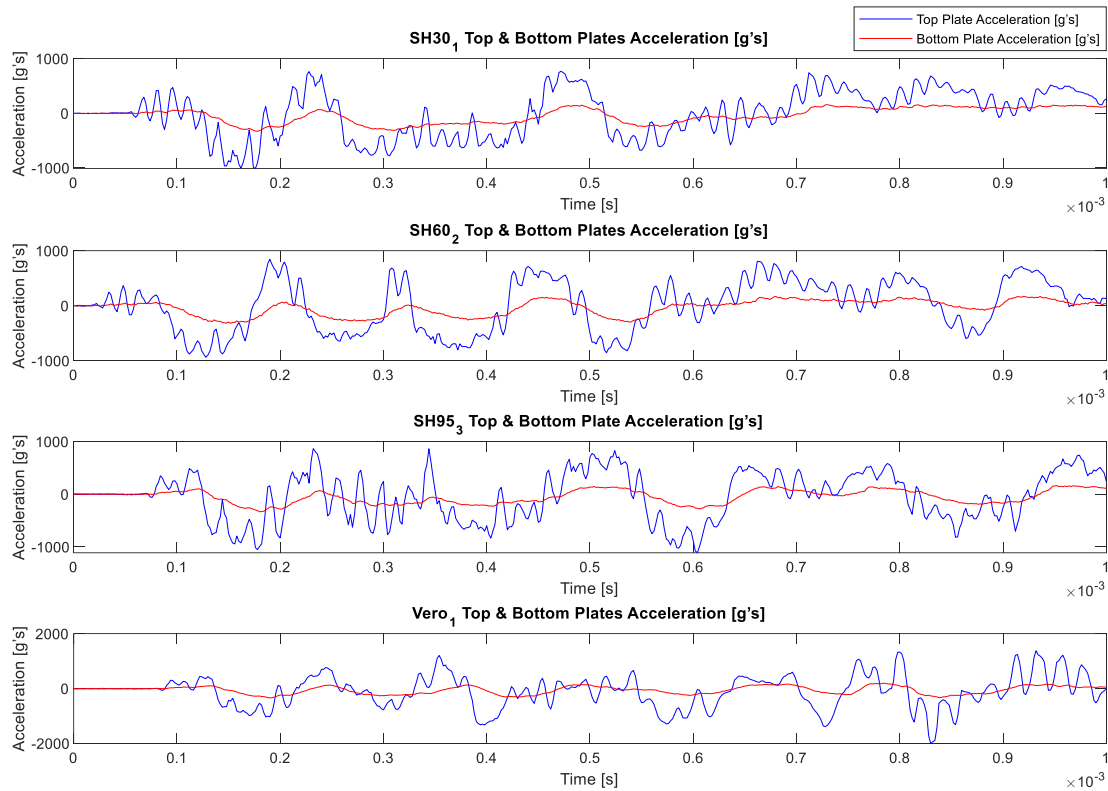
Figure 13: An acceleration reduction comparison between the four tested materials of the first 0.001 seconds after the impact.

CHAPTER THREE

THERMAL PERFORMANCE OF DIGITAL MATERIALS

The thermal performance of 3D printed photopolymers can significantly influence the mechanical properties of the resulting parts, as changes in temperature can lead to material expansion or contraction, causing dimensional changes and potential failure of the printed object [26]. A comprehensive understanding of the thermal behavior of 3D printed photopolymers is therefore essential for optimizing the printing process, improving the quality and reliability of the final product, and reducing the likelihood of part failure due to thermal stresses [27-28].

This chapter is organized as follows: In Section one, "Methodology," where the experimental setup is detailed, including the materials used, the laser source, and the measurement techniques applied. Section two, "Results and Discussion," presents the findings, analyzing the laser power meter results, the temperature distribution, and the energy delivered to the specimens.

3.1 Methodology

3.1.1 Laser Setup

The setup consists of a fiber coupled laser, laser power meter, a function generator, and a thermal camera.

BWF-2 Laser:

A continuous wave CW fiber-coupled laser from B&W TEK with the model number BWF-2 was utilized in this study. It has a core diameter of 400 m, a maximum output power of 250 mW, and a 532 nm (green) wavelength. Additionally, the laser features a flat top bean profile, a 0.22 NA beam divergence, and a IIIb CDRH laser class [29]. Through a connection attached to the DB-9 or BNC connector on the back panel, the laser can be controlled remotely. The SDG1032X function generator, a dual-channel waveform generator with a maximum bandwidth of 60 MHz, is connected to the laser in this configuration. [31].
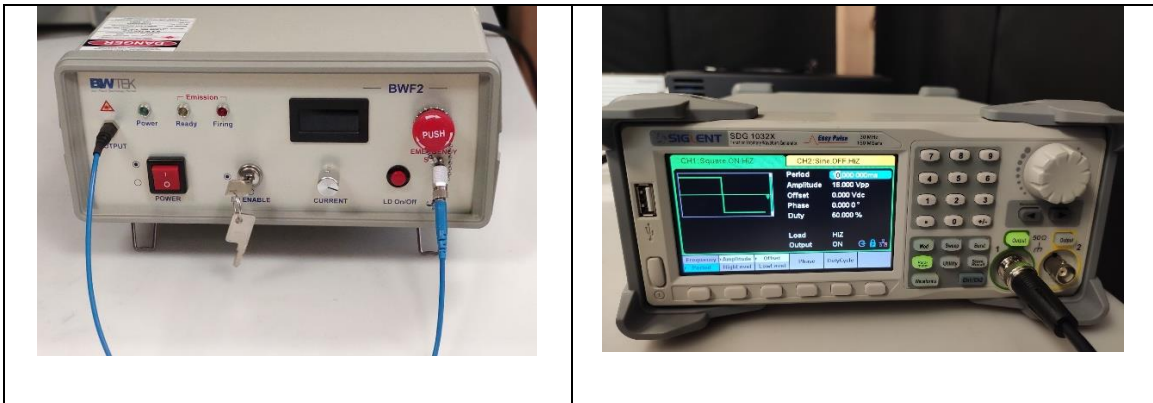
Figure 14: (A). BWF-2 fiber-coupled laser. (B). SDG1032X function generator

The power density of a continuous wave (CW) fiber-coupled laser was by dividing the laser's maximum output power by the cross-sectional area of the beam. Given the core diameter of 400 µm, the average power density of the laser can be calculated as the following:

$$Power\ Density = \frac{Output\ power}{Area}$$

$$Power\ Density = \frac{0.25}{\pi * (0.04\ /\ 2)^2} = 199\ W/cm^2$$

Where A = π * (d / 2)². This high average power density value indicates that the laser can deliver a significant amount of energy in a small area, making it a suitable choice for this experiment [4].

UP19K-30H-H5-INT-D0 Laser Power Meter

The thermal detector for laser power measurement is designed to handle a maximum average power of 30 W continuously, with a peak capacity of 60 W for 1-minute intervals. With a noise equivalent power of 1 mW, it operates within a broad spectral range of 0.193 - 20 μm, exhibiting a typical rise time of 0.6 s and a power sensitivity of 0.65 mV/W. The power calibration uncertainty is ±2.5%, while the repeatability is ±0.5%. The detector has a maximum average power density of 36 kW/cm² at 1064 nm and 10 W CW, and it features convection cooling with a 19 mm aperture diameter. [30]
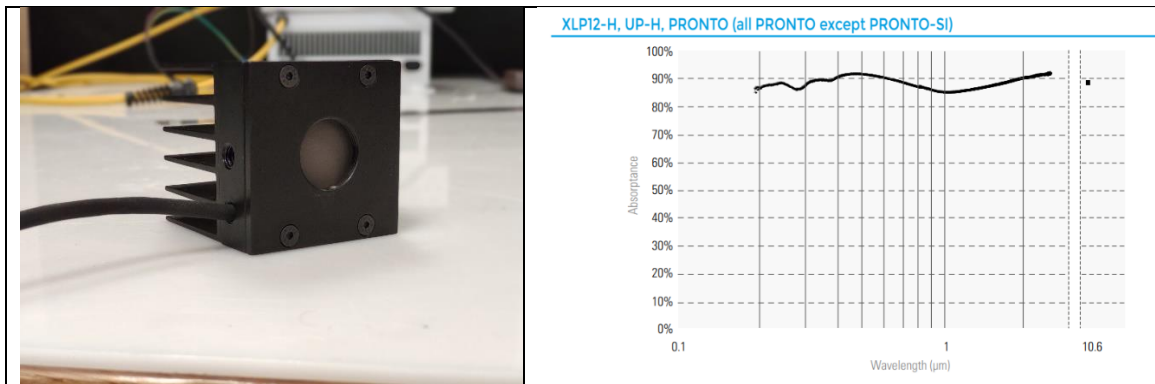
Figure 15: (A). UP19K-30H-H5-INT-D0 laser power meter. (B). laser power meter absorption curve.

Figure 15 (B) shows the absorption curve of the laser power meter. It's clear from the curve, the laser that has been used in this study falls within the wavelength that the device can detect with 90% absorptance.

FAST M350 Thermal Camera

The FAST M350 is a scientific thermal infrared camera from TELOPS that exhibits high-performance capabilities, Figure 16. It has a cooled InSb detector type and operates in the mid-wave infrared (MWIR) with a spectral range of 1.5 μm to 5.4 μm, a spatial resolution of 640 × 512 pixels, and a detector pitch of 15 μm. It has a frame rate of up to 355 Hz in full-frame mode, and 4,980 Hz at 132 x 4. The camera has a typical NETD of 20 mK and an exposure time of 0.5 μs to full frame rate [33]. The camera can be connected to the computer in order to save and record images and videos, also to have a real-time view through Revel IR software from TELOPS as well. The lens used with the camera is EL-7904 with focal length of 50 mm, and works within range of [0 – 350] °C.

Figure 16: FAST M350 Thermal Camera

Experimental Setup:

Figure 17 below shows the experimental setup, consists of thermal camera, fiber-coupled CW laser, function generator, power meter, and the tested sample. The Thermal camera was 80 cm away from the specimen to ensure recoding high-quality images with frame size of 388 x 260 pixels at 24 FPS. The tests' samples were 10 mm away from the laser output and exposed to the laser beam for at least 7 minutes.
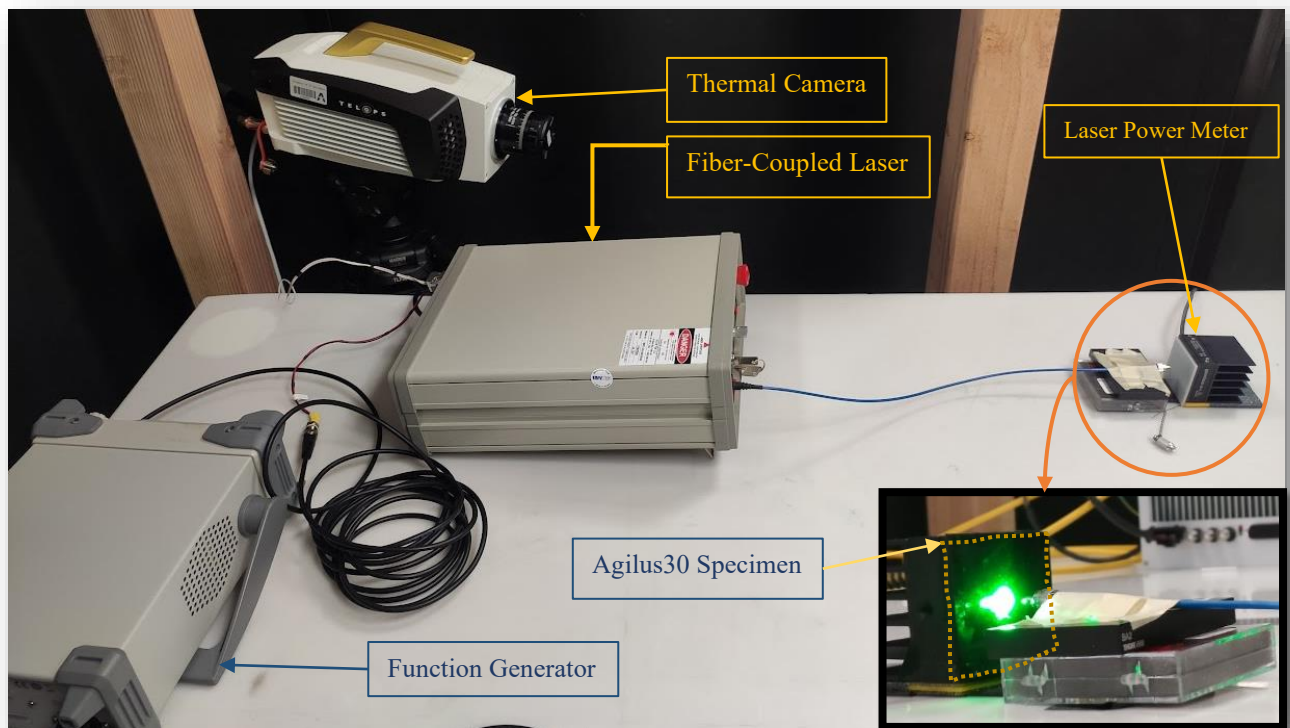
Figure 17: Experiment setup including thermal camera, fiber-coupled CW laser, function generator, power meter, and the tested sample.

3.1.2 Materials and Specimens Preparation:

Two materials were utilized for the samples tested in this study: Agilus30 Black and Digital ABS. All samples were 3D printed using a Stratasys J850 Prime polyjet printer. A glossy surface finish was chosen, which accounts for the shiny appearance in some of the sample, Figure 18 images in and

Table 4. Three distinct sets of samples were printed for subsequent testing. The first set consisted solely of Agilus30 Black with four different thicknesses (0.25 mm, 0.5 mm, 1 mm, and 2 mm). The second set of samples was printed using only Digital ABS, with the same thickness as the Agilus30 specimens. The third and final set combined both materials, with each constituting 50% of the total thickness which makes the sample made of two layers. These mixed samples were printed with three different thicknesses: 0.5 mm, 1 mm, and 2 mm. The bottom half of each sample was initially covered with support material, which was later removed to prepare the samples for testing. The Stratasys J850 Prime employs SUP706B™ as a water-soluble support material.
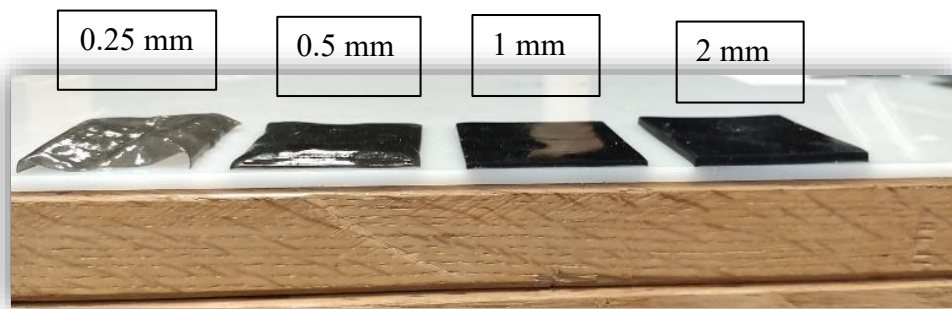
Figure 18: Agilus30 samples with different thicknesses used in the study.

The samples used in the experiment were square in shape, measuring 50.8 by 50.8 mm, with varying thicknesses as described earlier. GrabCAD Print™ is the software used to communicate with the printer and manage material selection and printing instructions. Finally, all samples were designed using SOLIDWORKS software.

$L = 50.8$ mm
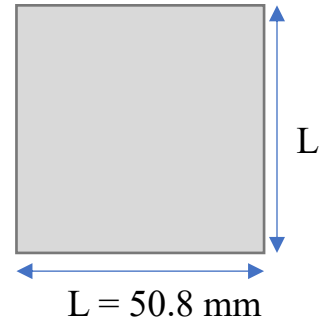
Table 4: Tested samples made from Agilus30 and Digital ABS, 50% each of the total thickness.

Thickness [mm]		
0.5	1	2
Digital ABS facing up		
Agilus30 facing up		
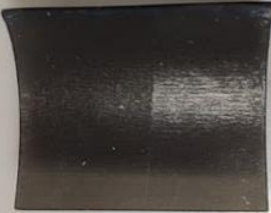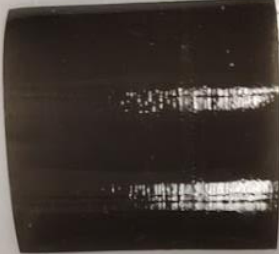
3.2 Results and Discussion

In this study, numerous preliminary findings were obtained that require validation. Nonetheless, these results contribute to a more comprehensive understanding of the materials' thermal properties and their performance under directed energy sources. The laser power meter results revealed a decrease in the maximum power reaching the meter input when covered by samples of varying thicknesses. Moreover, the recorded surface temperature and irradiance of the specimens by the thermal camera provided valuable insights into the heating rates of different materials and the energy delivered to their surfaces.

3.2.1 Laser Power Meter

Initially, the laser beam was measured by positioning the laser power meter 10 mm away from the laser output, as shown in Figure 4, without any obstructions blocking the power meter input. The meter was exposed to the laser beam for a sufficient duration to ensure consistent maximum

power readings. The output power, displayed in Figure 19 (A), was 220 mW at that distance, and this value will be utilized for further calculations in subsequent sections.
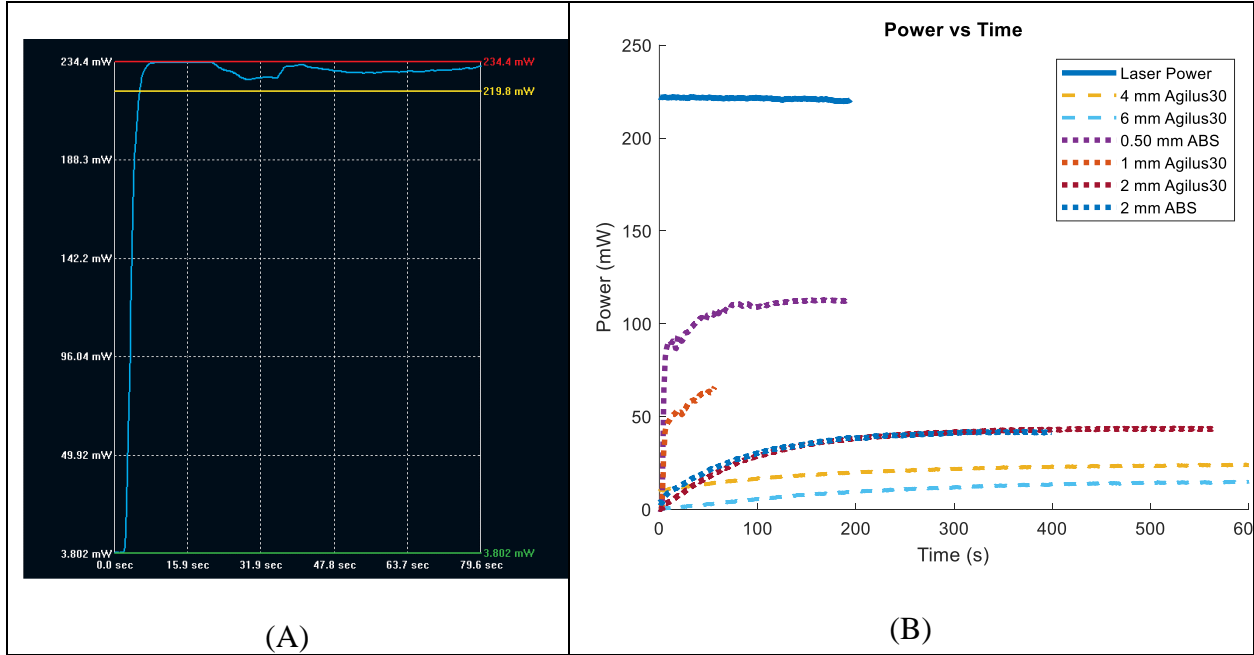
Figure 19: (A). Laser power meter measurements of the laser beam. Power in (mW) V.S Time in (s). (B). Power curves for different materials at different thicknesses.

Figure 19 (B) depicts the power versus time curves for different materials recorded using the laser meter. Starting with the "Laser Power," it represents the laser beam power illustrated in Figure 19 (A). The Agilus30 4 mm and 6 mm curves represent the power readings obtained after covering the meter input with samples made from Agilus30 at these thicknesses. It is evident that thickness significantly affects the reduction of maximum power measured by the meter. At 4 mm, the measured power is 24 mW, which is nine times less than the maximum power. For 6 mm, the power is 14 mW, which is nearly 16 times less than the maximum power. The remaining curves are for the two-layer samples. "0.5 mm ABS" refers to a sample composed of two materials, with each contributing 50% to the total thickness, as explained earlier, but with Digital ABS facing the laser beam. The same applies to the samples with Agilus30 in their names;

46

for example, "1 mm Agilus30" refers to a sample made from the two materials with Agilus30 facing the laser beam. The curves indicate that doubling the sample thickness results in a nearly halved power measurement, which is also consistent with the observations for 4 mm and 6 mm samples. It is worth mentioning that "0.5 mm Agilus30" and "1 mm ABS" were not plotted due to data export issues from one format to another. Nevertheless, their power versus time curves, obtained from the laser meter software, display similar curves for ABS and Agilus30 with the same thicknesses, respectively. This can be observed in the 2 mm sample thickness, where both Agilus30 and ABS exhibit identical performance.

Table 5: Summary of the average power and time of three tested samples of made of Agilus30 of each thickness.

Sample Thickness	Average Power [mW]	Average Test Duration [s]	Average Time to Reach Steady State [s]
0.25 mm	112	437	40
0.5 mm	86	493	60
1 mm	52	473	80
2 mm	40	515	150

Table 5 summarizes the data collected from the power vs time curves for Agilus30 from the laser meter software like Figure 19 (A). The tables' data show consistency with what being observed from Figure 19 despite the fact that the other samples were made from mixed materials. And since the 4 mm, and 6 mm samples in the graph above were made from pure Agilus30. It can be seen that the relation between the thickness and the measured power is inversely proportional by almost half.

3.2.2 Temperature and Irradiance Measurements

Understanding the transmission of power through the tested materials, as discussed in the previous section, is crucial. Equally important is comprehending how the materials' surfaces react to directed energy. The thermal camera greatly facilitated this understanding by providing temperature and irradiance data, which is the amount of power delivered by a surface per unit area, for all tested samples. This information significantly enhanced our understanding of the materials' performance.

Figure 20 illustrates the temperature vs time curves of Agilus30 at various thicknesses, ranging from 0.25 to 2 mm. These data represent the maximum temperature experienced by the sample surfaces while exposed to the laser beam. It is evident that thickness plays a major role in surface temperature. The 1 mm thickness experienced the highest temperature among all samples, followed by the 0.5 mm and 2 mm thicknesses, which exhibit similar trends. However, the 2 mm samples required more time to reach steady state, which align with the results in Table 5. The lowest temperature among the four tested thicknesses was observed in the 0.25 mm sample, but it also reached steady state the fastest. This is due to its small thickness, which allows the majority of the laser power to pass through the sample, as demonstrated in Figure 19 and Table 5.
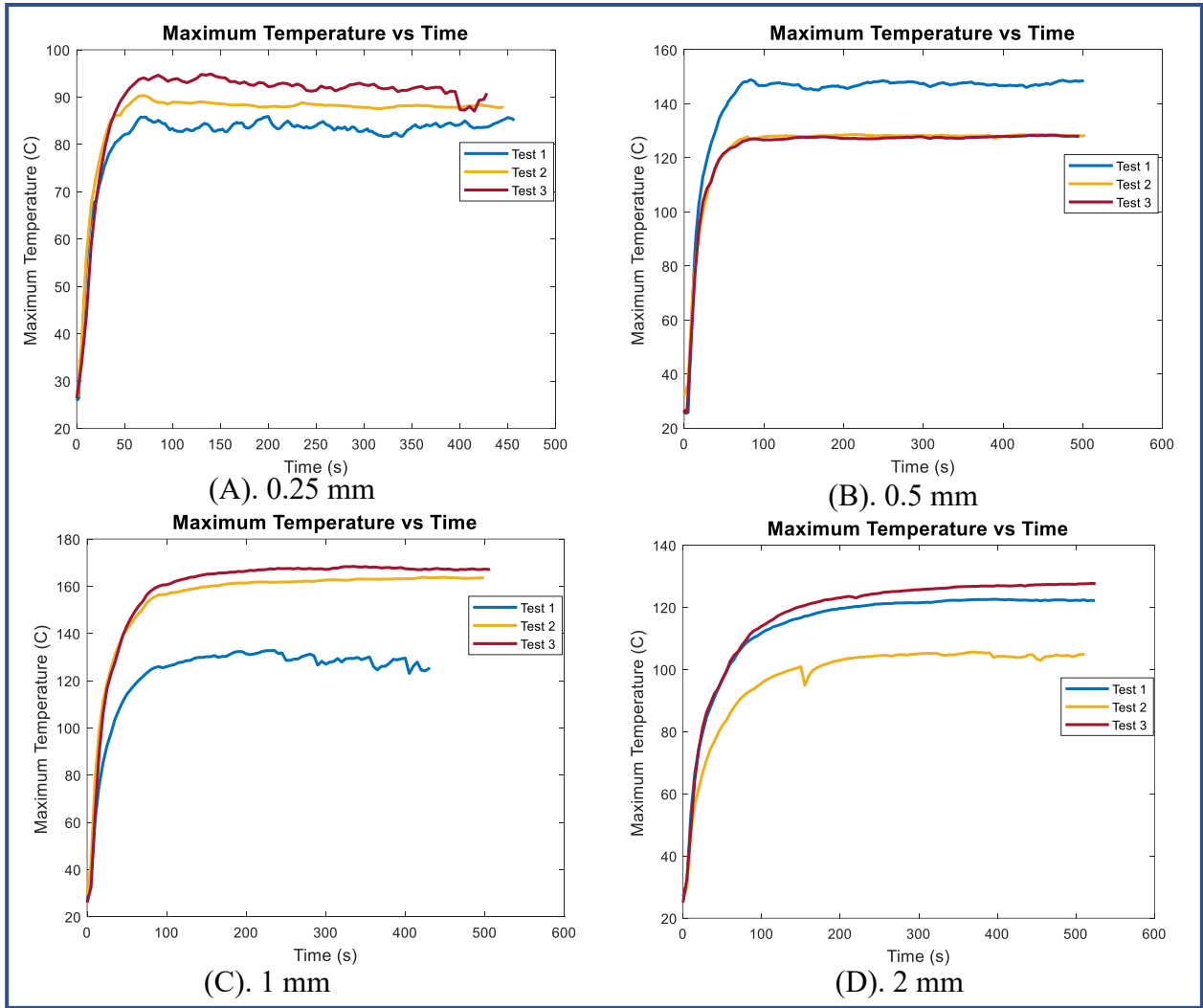
Figure 20: The maximum temperature in degrees Celsius (°C) that was recorded vs time in each test of the 4 different thicknesses, by using the thermal camera. (A). Temperature vs Time curves of 0.25 mm thickness samples. (B). Temperature vs Time curves of 0.5 mm thickness samples. (C). Temperature vs Time curves of 1 mm thickness samples. (C). Temperature vs Time curves of 2 mm thickness samples.

Following the same testing procedure of Agilus30 samples, Table 6 displays temperature and irradiance readings for each sample at three different locations. These locations can be seen in Figure 21. Starting with area D_1, which is the smallest among the three, followed by D_2, and finally,

the "Full Sample" that was within the camera's field of view. Figure 21 provides just an example of how the camera interacts with the sample surface.

All data presented in Table 6 were obtained from the two-layer samples, adhering to the same naming convention as Figure 19 (B). The right side of the table represents when Digital ABS faced the
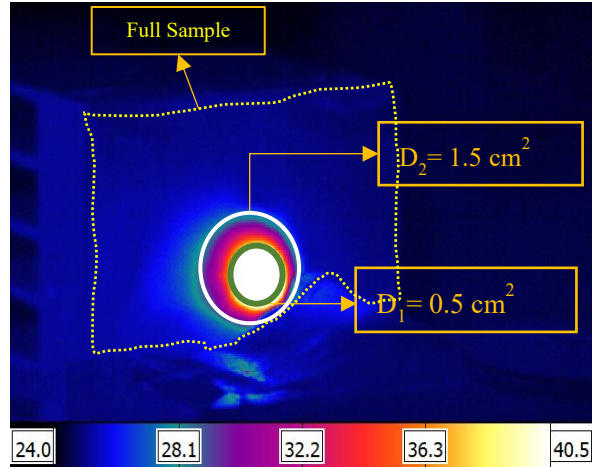
Figure 21:: Thermal camera image showing the different areas that are used for the calculation.

laser beam, while the left side corresponds to when Agilus30 faced the laser beam. Three different readings for both temperature (°C) and irradiance (in W/m^2) were recorded. The maximum values indicate when the sample surface experienced the highest temperature, which consequently corresponds to the highest irradiance. Additionally, the mean temperature and irradiance over the course of the entire test for both areas D_1 and D_2 are reported. It is worth noting the relatively small difference in average readings between D_1 and D_2, given the minor change in the tested area. Therefore, the average data for the "Full Sample" is not reported, as it is insignificant compared to the other regions.

Table 6: Temperature and Irradiance readings of 8 different 2 layers mixed materials with different thicknesses

	Tested Material							
	Agilus30					*Digital ABS*		
Thickness [mm]	0.5	1	2	4	6	0.5	1	2
Temperature [°C]								
Max	221.2	275.1	119	107.8	172.7	110	158	80.2
Mean D_1	73.1	69.7	61.8	61.7	74.8	67.8	79.9	56.4
Mean D_2	34.6	33.6	35.7	36.7	42.145	41.2	44.3	36.6
Irradiance [W/m^2]								
Max	13.5	27	2.19	1.71	6.27	1.79	4.82	0.86
Mean D_1	1.15	1.28	0.61	0.58	1.03	0.68	1.08	0.45
Mean D_2	0.32	0.35	0.27	0.27	0.39	0.33	0.41	0.25

Figure 22 -Figure 25 illustrate a comparison in the temperature and irradiance vs time for 0.25 mm, 0.5 mm, 1 mm, and 2 mm pure Agilus30 Black samples using the thermal camera. Part (A) of each figure presents the average temperature vs. time curves at three different regions. D_1 and D_2 show similar data to that was shared in Table 6 above, however, average sample temperature was plotted here in order to compare it to other regions. From the numbers, it can be observed that the overall change in the sample's temperature is insignificant compared to the ambient temperature. The color scale at the bottom of each picture in part (C) shows the temperature gradient. Both pictures in (C) are for the same sample, and by using a feature in Revel IR software (the thermal camera software) called Extended High Dynamic Range Imaging (EHDRI), which is a control subcategory that allows the user to specify several exposure times to be used sequentially during an acquisition. EHDRI provides more accuracy to the recorded data, which is why it was used in this study.

Figure 22: Test 3 of Agilus30 sample with 0.25 mm thickness. (A) Mean temperature vs. time curve. (B) Irradiance vs. time curve. (C) Thermal camera image showing the different areas used for calculating temperature and irradiance.
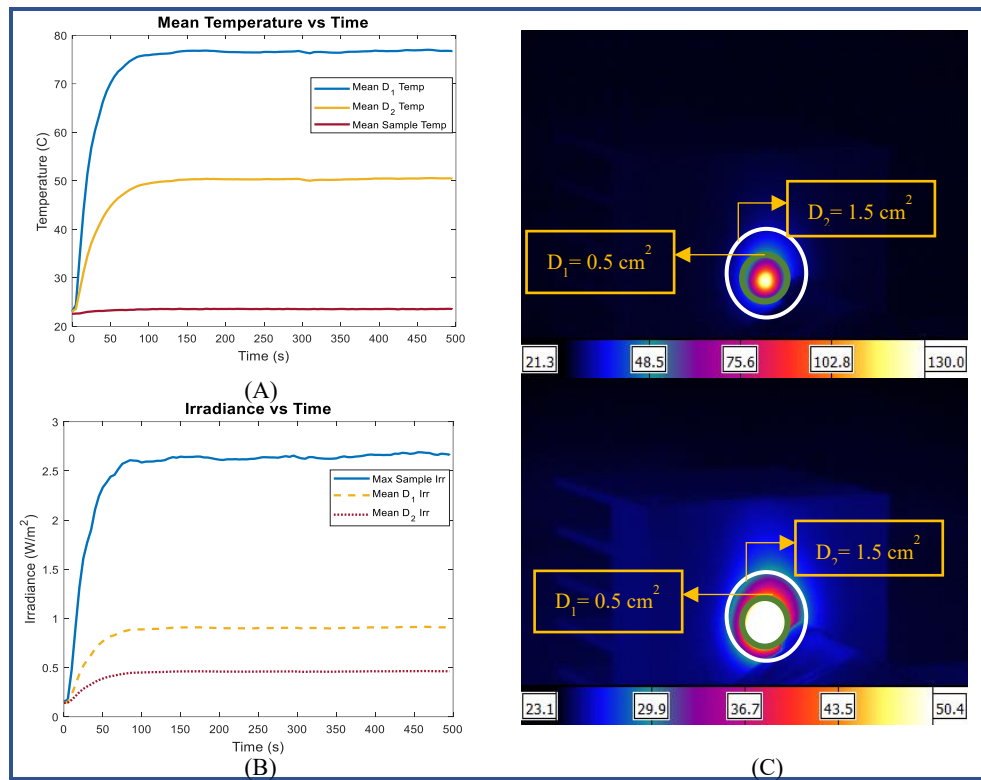
Figure 23: Test 3 of Agilus30 sample with 0.50 mm thickness. (A) Mean temperature vs. time curve. (B) Irradiance vs. time curve. (C) Thermal camera image showing the different areas used for calculating temperature and irradiance.

Figure 24: Test 3 of Agilus30 sample with 1 mm thickness. (A) Mean temperature vs. time curve. (B) Irradiance vs. time curve. (C) Thermal camera image showing the different areas used for calculating temperature and irradiance.
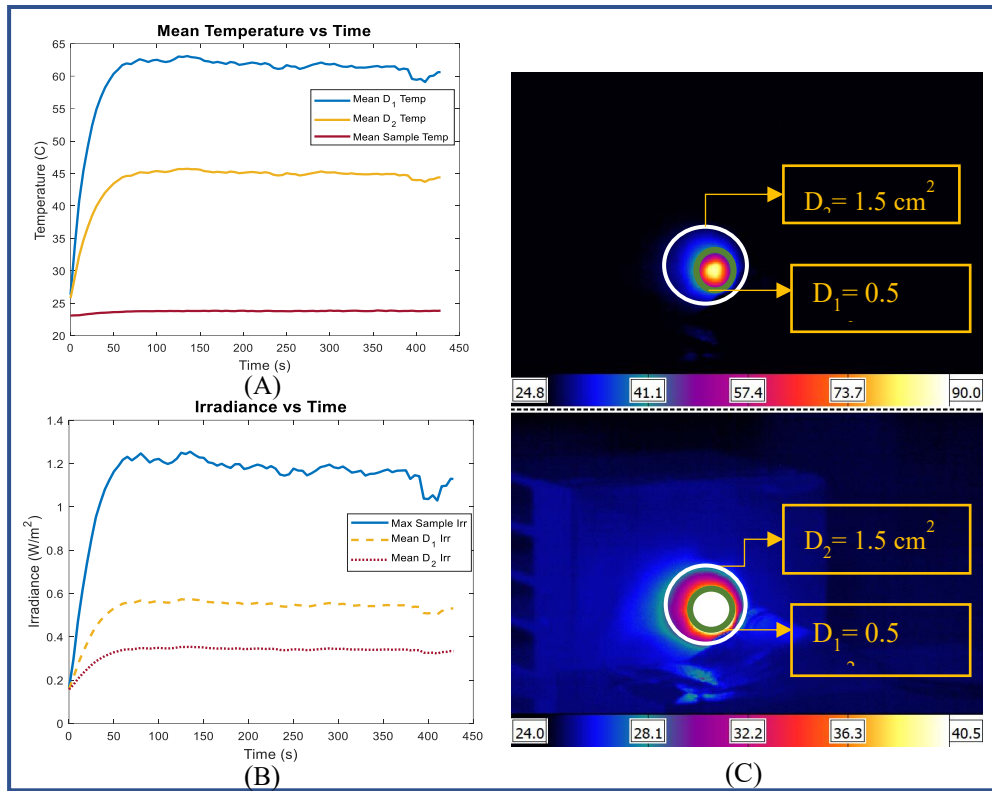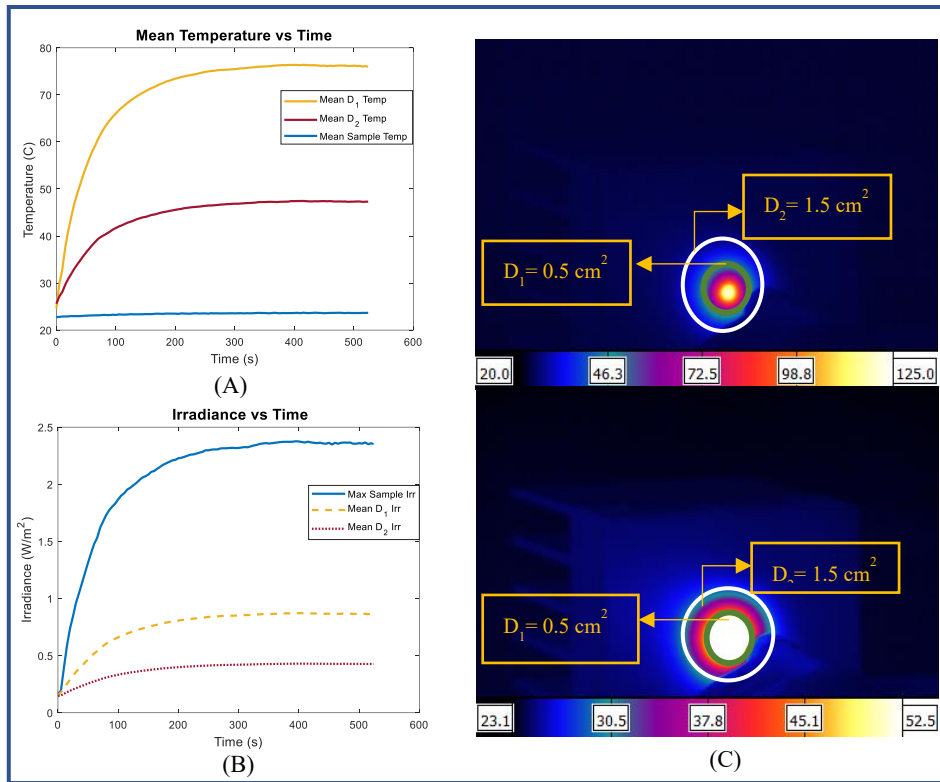
Figure 25: Test 3 of Agilus30 sample with 2 mm thickness. (A) Mean temperature vs. time curve. (B) Irradiance vs. time curve. (C) Thermal camera image showing the different areas used for calculating temperature and irradiance.
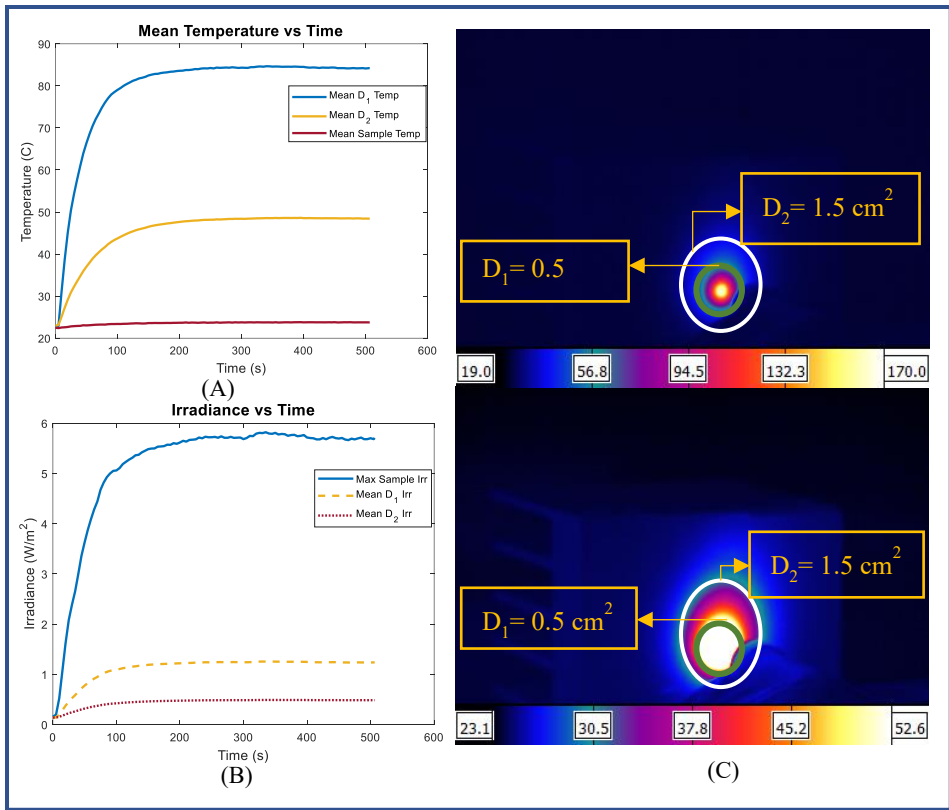
In each Figure 22 -Figure 25, part (B) displays the irradiance versus time for two regions, as well as the maximum irradiance experienced by the sample during the testing period. The irradiance data, generally speaking, replicate the temperature ones as the curves suggests.

Having this important data enables the calculation of both heating rate and the energy delivered to the sample's surface. By differentiating the temperature vs time curves, the heating rate calculations can be performed. Additionally, calculating the area under the irradiance curves allows for the determination of the energy delivered to sample's surface. It is interesting to observe the variations in heating rates for the regions considered in this study. It is clear that the rates are

closely related within the same location, despite the fact that the temperature differences experienced by these samples with various thicknesses were quite substantial.

Table 7: The average heating rate at 3 different surfaces areas and the energy delivered to the sample surface.

Sample Thickness	Average Heating rate [°C/s]			Energy Delivered [J/m^2]
	D_1	D_2	Full Sample	
0.25 mm – Test 3	0.08	0.043	0.0018	483.3
0.5 mm – Test 3	0.108	0.054	0.0012	1239.7
1 mm – Test 3	0.12	0.05	0.0025	2617.8
2 mm – Test 1	0.098	0.041	0.0017	1086.1

CHAPTER FOUR

CONCLUSION AND FUTURE WORK

This study has explored the mechanical and thermal properties of hybrid materials manufactured using Agilus30 Black and VeroMagentaV, as well as 3D printed digital materials, such as Digital ABS, under various conditions. The mechanical properties of hybrid materials with Shore A hardness values of 30, 60, and 95 were assessed through tensile testing and drop tower impact tests. Meanwhile, directed energy sources like lasers were employed to evaluate thermal performance. The results from mechanical properties testing underscored the significance of material properties, defect attributes, and mechanical responses in determining hybrid materials' performance. Each hybrid material exhibited distinct mechanical behaviors, with SH95 displaying characteristics similar to plastic, owing to its rigidity and elevated fracture stress. In contrast, SH30 and SH60 demonstrated flexibility and elongation. Moreover, the reduction in acceleration observed in drop tower impact tests displayed a nonlinear correlation with the concentration of Agilus30, emphasizing the complex relationship between material composition and mechanical behavior.

Regarding thermal performance, laser meter findings revealed a decline in maximum power reaching the meter input as sample thickness increased. Temperature distribution analysis found no direct correlation between thickness and peak surface temperature. Although the study's findings are preliminary, they contribute to a more in-depth understanding of materials' mechanical and thermal properties and their behavior under different conditions.

In summary, this research enhances our knowledge of hybrid and 3D printed materials' characteristics and provides a direction for future investigations on material selection, optimization, and component design. By examining the relationships between material properties, mechanical performance, flaw attributes, energy absorption potential, and thermal behavior, researchers and engineers can optimize these materials to meet the ever-changing demands of contemporary technological and engineering applications.

Future work should prioritize further validation of the findings and expanding the range of mechanical tests and investigations. Tensile testing should include additional samples at slower and faster strain rates to better comprehend the materials. Introducing more defects of varying shapes and locations could also contribute to a better understanding of these hybrid materials. For dynamic impact tests, different cube sizes should be considered, as the materials' composition is not linearly related. Static impact tests might also offer insights into material behavior, as static performance may not necessarily indicate dynamic performance and vice versa. Simulation studies can be valuable in validating results and understanding potential interactions. Enhancements to the experimental setup should also be explored, such as employing digital image correlation (DIC) for both impact and tensile tests, especially for samples with defects. In this study, the speckle pattern was suboptimal for producing useful data, so addressing this issue will be crucial for future investigations.

Finally, future work should investigate improvements to thermal performance evaluation. This might involve using an optical table for a vibration-free environment, incorporating laser mirrors, lenses, and additional optical components for better data collection, and utilizing lasers with varying wavelength ranges and powers to simulate real-life situations. Conducting simulation studies of laser radiation interaction can be beneficial in predicting interactions between laser radiation and different materials, as well as evaluating potential damage risks [38]. Simulation studies can save time, provide more options for testing various materials, and help reduce costs while concentrating on the most effective alternatives.

Acknowledgment

REFERENCES

[1]. Smith, J., Petrovic, P., Rose, M., De Souz, C., Muller, L., Nowak, B., & Martinez, J. (2021). Placeholder Text: A Study. The Journal of Citation Styles, 3. https://doi.org/10.10/X

[2]. Martorelli, M., Gloria, A., Bignardi, C., Calì, M., & Maietta, S. (2020). Design of Additively Manufactured Lattice Structures for Biomedical Applications. Journal of Healthcare Engineering, 2020. https://doi.org/10.1155/2020/2707560

[3]. Wohlers, T., & Gornet, T. (2014). History of Additive Manufacturing 2014. Wohlers Report 2014 - 3D Printing and Additive Manufacturing State of the Industry, 1–34.

[4]. Wickramasinghe, S., Do, T., & Tran, P. (2020, July 1). FDM-Based 3D printing of polymer and associated composite: A review on mechanical properties, defects and treatments. Polymers. MDPI AG. https://doi.org/10.3390/polym12071529

[5]. Ahn, S. H., Montero, M., Odell, D., Roundy, S., & Wright, P. K. (2002). Anisotropic material properties of fused deposition modeling ABS. Rapid Prototyping Journal, 8(4), 248–257. https://doi.org/10.1108/13552540210441166

[6]. Nomani, J., Wilson, D., Paulino, M., & Mohammed, M. (2020). Effect of layer thickness and cross-section geometry on the tensile and impact properties of 3D printed ABS. Materials today communications, 22, 100626.

[7]. Algarni, M., & Ghazali, S. (2021). Comparative Study of the Sensitivity of PLA, ABS, PEEK, and PETG's Mechanical Properties to FDM Printing Process Parameters. Crystals.

[8]. Tee, Y.L., Tran, P., Leary, M., Pille, P., & Brandt, M. (2020). 3D Printing of polymer composites with material jetting: Mechanical and fractographic analysis. Additive manufacturing, 36, 101558.

[9]. Grimaldo Ruiz, O., Rodriguez Reinoso, M., Ingrassia, E., Vecchio, F., Maniero, F., Burgio, V., Civera, M., Bitan, I., Lacidogna, G., & Surace, C. (2022). Design and Mechanical Characterization Using Digital Image Correlation of Soft Tissue-Mimicking Polymers. Polymers, 14.

[10]. Shaukat, U., Rossegger, E., & Schlögl, S. (2022). A Review of Multi-Material 3D Printing of Functional Materials via Vat Photopolymerization. Polymers, 14.

[11]. Jackson, A., Ahmad, L. M., Adnan, A. (2023). "On the Static and Dynamic Energy Absorption of Additively Manufactured Lattice Structures"

[12]. Nath, S. D., & Nilufar, S. (2020). An Overview of Additive Manufacturing of Polymers and Associated Composites. Polymers, 12(11), 2719. https://doi.org/10.3390/polym121127196587/abe353

[13]. Gao, W., Zhang, Y., Ramanujan, D., Ramani, K., Chen, Y., Williams, C. B., … Zavattieri, P. D. (2015). The status, challenges, and future of additive manufacturing in engineering. CAD Computer Aided Design, 69, 65–89. https://doi.org/10.1016/j.cad.2015.04.001

[14]. Gibson, I., Rosen, D., & Stucker, B. (2015). Additive Manufacturing Technologies: 3D Printing and Direct Digital Manufacturing, Springer, New York. Johnson Matthey Technology Review, 59(3), 498.

[15]. Sheng, R. (2022). 3D Printing: A Revolutionary Process for Industry Applications. 3D Printing: A Revolutionary Process for Industry Applications (pp. 1–192). Elsevier. https://doi.org/10.1016/C2021-0-02154-4

[16]. Stansbury, J. W., & Idacavage, M. J. (2016). 3D printing with polymers: Challenges among expanding options and opportunities. In Dental Materials (Vol. 32, pp. 54–64). Elsevier Inc. https://doi.org/10.1016/j.dental.2015.09.018

[17]. Wei, X., Zou, N., Zeng, L., & Pei, Z. (2022). PolyJet 3D printing: Predicting color by multilayer perceptron neural network. Annals of 3D Printed Medicine, 5, [100049]. https://doi.org/10.1016/j.stlm.2022.100049

[18]. Agaliotis, E.M., Ake-Concha, B.D., May-Pat, A., Morales-Arias, J.P., Bernal, C., Valadez-González, A., Herrera-Franco, P.J., Proust, G., Koh-Dzul, J.F., Carrillo, J.G., & Flores-Johnson, E.A. (2022). Tensile Behavior of 3D Printed Polylactic Acid (PLA) Based Composites Reinforced with Natural Fiber. Polymers, 14.

[19]. Cojocaru, V.D., Frunzaverde, D., Nedelcu, D., Micloșină, C.O., & Mărginean, G. (2021). Study Regarding the Influence of the Printing Orientation Angle on the Mechanical Behavior of Parts Manufactured by Material Jetting. Materiale Plastice.

[20]. Pugalendhi, A., Ranganathan, R., & Ganesan, S. (2020). Impact of process parameters on mechanical behaviour in multi-material jetting. Materials Today: Proceedings.

[21]. ASTM D638-14 (2014) Standard Test Method for Tensile Properties of Plastics. ASTM International, West Conshohocken. http://www.astm.org.

[22]. Vero material data sheet PDF | Stratasys - . (n.d.). Retrieved April 2, 2023, from https://www.stratasys.com/contentassets/ab69196d173842cca634d07febba0f10/mds_pj_vero_0221a-2.pdf?v=4a1902

[23]. The Stratasys J850 Prime PolyJet 3D printer. (n.d.). Retrieved April 2, 2023, from https://stratasys-corporate-prod-

slot.dxc.stratasys.com/contentassets/f5e7f8431584452abfd3f73ac2ab489d/br_pj_j8seriesbrochure_0522a.pdf?v=4aa449

[24]. Zorzetto, L., Andena, L., Briatico-Vangosa, F., De Noni, L., Thomassin, J., Jérôme, C., Grossman, Q., Mertens, A., Weinkamer, R., Rink, M., & Ruffoni, D. (2020). Properties and role of interfaces in multimaterial 3D printed composites. Scientific Reports, 10.

[25]. Lumpe, T.S., Mueller, J., & Shea, K. (2019). Tensile properties of multi-material interfaces in 3D printed parts. Materials & Design.

[26]. Ligon, S. C., Liska, R., Stampfl, J., Gurr, M., & Mülhaupt, R. (2017). Polymers for 3D Printing and Customized Additive Manufacturing. Chemical reviews, 117(15), 10212–10290. https://doi.org/10.1021/acs.chemrev.7b00074

[27]. Gokuldoss, P. K., Kolla, S., & Eckert, J. (2017). Additive Manufacturing Processes: Selective Laser Melting, Electron Beam Melting and Binder Jetting-Selection Guidelines. Materials (Basel, Switzerland), 10(6), 672. https://doi.org/10.3390/ma10060672

[28]. Sing, S. L., An, J., Yeong, W. Y., & Wiria, F. E. (2016). Laser and electron-beam powder-bed additive manufacturing of metallic implants: A review on processes, materials and designs. Journal of orthopaedic research : official publication of the Orthopaedic Research Society, 34(3), 369–385. https://doi.org/10.1002/jor.23075

[29]. 532nm 0 - 250MW, fiber-coupled laser: Edmund Optics. Edmund Optics Worldwide. (n.d.). Retrieved April 30, 2023, from https://www.edmundoptics.com/p/532nm-0-250mw-fiber-coupled-laser/2814/

[30]. UP19K-30H-H5-D0 - thermopile laser power detector. Gentec. (n.d.). Retrieved April 30, 2023, from https://www.gentec-eo.com/products/up19k-30h-h5-d0

[31]. SDG1000X waveform generators: Siglent Function Generator. Siglent. (2022, June 27). Retrieved April 30, 2023, from https://siglentna.com/waveform-generators/sdg1000x-series-functionarbitrary-waveform-generators/

[32]. Xiang, Z., Yin, M., Dong, G., Mei, X., & Yin, G. (2018). Modeling of the thermal physical process and study on the reliability of linear energy density for selective laser melting. Results in Physics, 9, 939–946. https://doi.org/10.1016/j.rinp.2018.03.047

[33]. Scientific Thermal Infrared Camera. - telops. (n.d.). Retrieved May 1, 2023, from https://www.telops.com/wp-content/uploads/2021/06/2021-fast-m350-brochure.pdf

[34]. Saghafi, S., Withford, M. J., & Ghoranneviss, Z. (2006). Characterizing flat-top laser beams using standard beam parameters. Canadian Journal of Physics, 84(3), 223–240. https://doi.org/10.1139/p06-012

[35]. Fathi, H., Närhi, M., & Gumenyuk, R. (2021). Towards ultimate high-power scaling: Coherent beam combining of fiber lasers. Photonics, 8(12), 566. https://doi.org/10.3390/photonics8120566

[36]. Kasai, Y., Aizawa, T., & Tanaka, D. (2018). High-power fiber-coupled pump lasers for fiber lasers. High-Power Diode Laser Technology XVI. https://doi.org/10.1117/12.2288139

[37]. Blanc, P., Espinar, B., Geuder, N., Gueymard, C., Meyer, R., Pitz-Paal, R., Reinhardt, B., Renné, D., Sengupta, M., Wald, L., & Wilbert, S. (2014). Direct normal irradiance related definitions and applications: The circumsolar issue. Solar Energy, 110, 561–577. https://doi.org/10.1016/j.solener.2014.10.001

[38]. Milovich, J. L., Jones, O. S., Berger, R. L., Kemp, G. E., Oakdale, J. S., Biener, J., Belyaev, M. A., Mariscal, D. A., Langer, S., Sterne, P. A., Sepke, S., & Stadermann, M. (2021). Simulation studies of the interaction of laser radiation with additively manufactured foams. Plasma Physics and Controlled Fusion, 63(5), 055009. https://doi.org/10.1088/1361-

APPENDIX

Table 8: Agilus30 Black Hybrid Material - Material Composition and Print Time.

	1X1X1 inch Cube	2X2X2 inch Cube	3X3X3 inch Cube	4X4X4 inch Cube	5X5X5 inch Cube
Print Time	2h 2m	5h 32m	13h 18m	18h 14m	1d 8h 20m
Total Materials (g)	73	332	967	1,959	3,713
Total Support (g)	10	31	71	107	182
Agilus30Black	30	204	658	1,534	2,955
Agilus30Clear	7	21	51	70	125
RGD515	7	21	51	70	125
RGD531	7	21	51	70	125
VeroBlackPlus	7	21	51	70	125
VeroClear	7	21	51	70	125
VeroPureWhite	8	23	54	75	133
SUP706	10	31	71	107	182
Agilus30:Total	0.5068	0.6777	0.7332	0.8188	0.8295

Table 9: SH60 Hybrid Material - Material Composition and Print Time.

	1X1X1 inch Cube	2X2X2 inch Cube	3X3X3 inch Cube	4X4X4 inch Cube	5X5X5 inch Cube
Print Time	2h 2m	5h 32m	13h 18m	18h 15m	1d 8h 55m
Total Materials (g)	74	332	984	1,966	3,775
Total Support (g)	10	31	72	107	185
Agilus30Black	30	197	650	1,482	2,889
Agilus30Clear	7	21	51	70	127
RGD515	7	21	51	70	127
RGD531	7	21	51	70	127
VeroBlackPlus	8	28	76	129	242
VeroClear	7	21	51	70	127
VeroPureWhite	8	23	54	75	136
SUP706	10	31	72	107	185
Agilus:Total	0.5	0.6566	0.7124	0.7894	0.7989

Table 10: SH95 Hybrid Material - Material Composition and Print Time.

	1X1X1 inch Cube	2X2X2 inch Cube	3X3X3 inch Cube	4X4X4 inch Cube	5X5X5 inch Cube
Print Time	2h 2m	5h 44m	13h 19m	18h 15m	1d 9h 27m
Total Materials (g)	75	347	1,000	2,004	3,836
Total Support (g)	10	32	73	108	188
Agilus30Black	25	159	512	1,156	2,234
Agilus30Clear	7	22	51	70	129
RGD515	7	22	51	70	129
RGD531	7	22	51	70	129
VeroBlackPlus	14	76	230	492	948
VeroClear	7	22	51	70	129
VeroPureWhite	8	24	54	76	138
SUP706	10	32	73	108	188
Agilus:Total	0.4267	0.5216	0.563	0.6118	0.6160
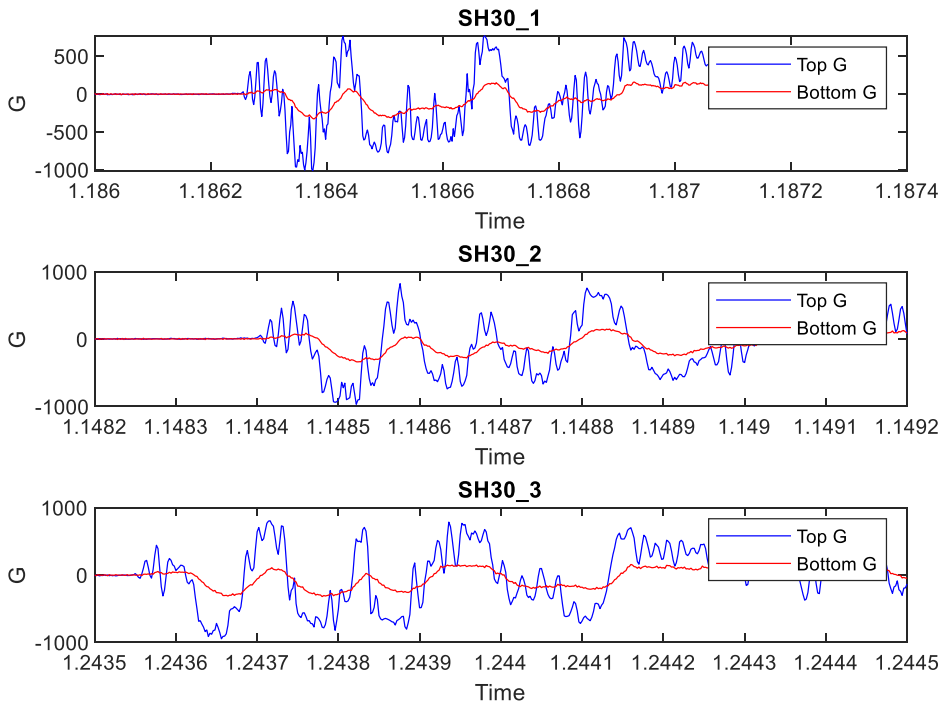
Figure 26:The acceleration reduction of the Agilus30 specimens at the moment of the impact under the drop tower at 2 m/
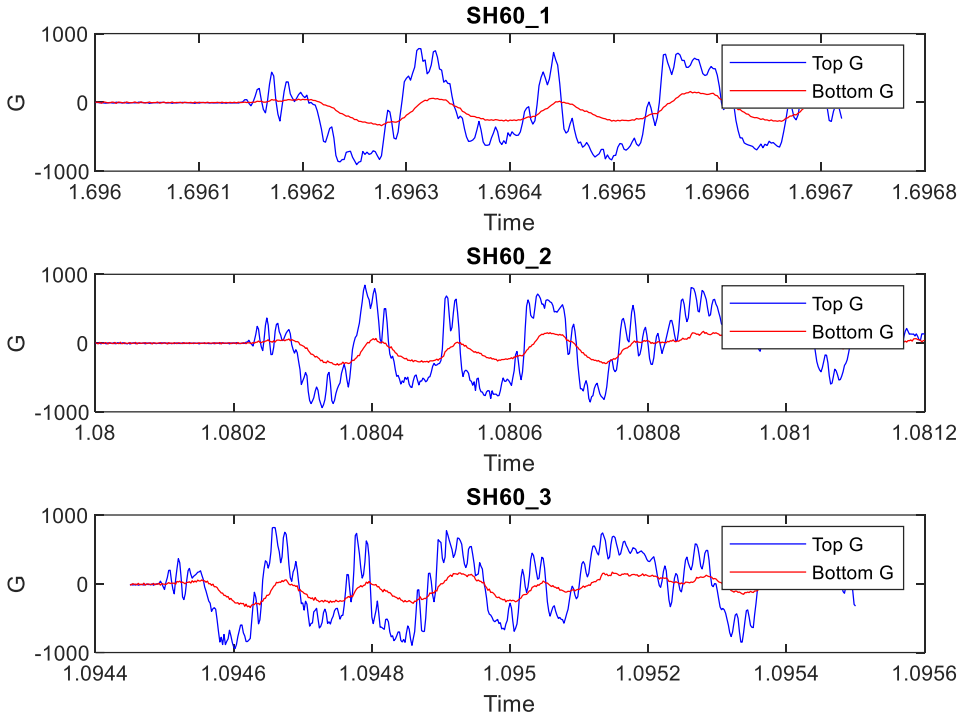
Figure 27:The acceleration reduction of the hybrid material SH60 specimens at the moment of the impact under the drop tower at 2 m/s
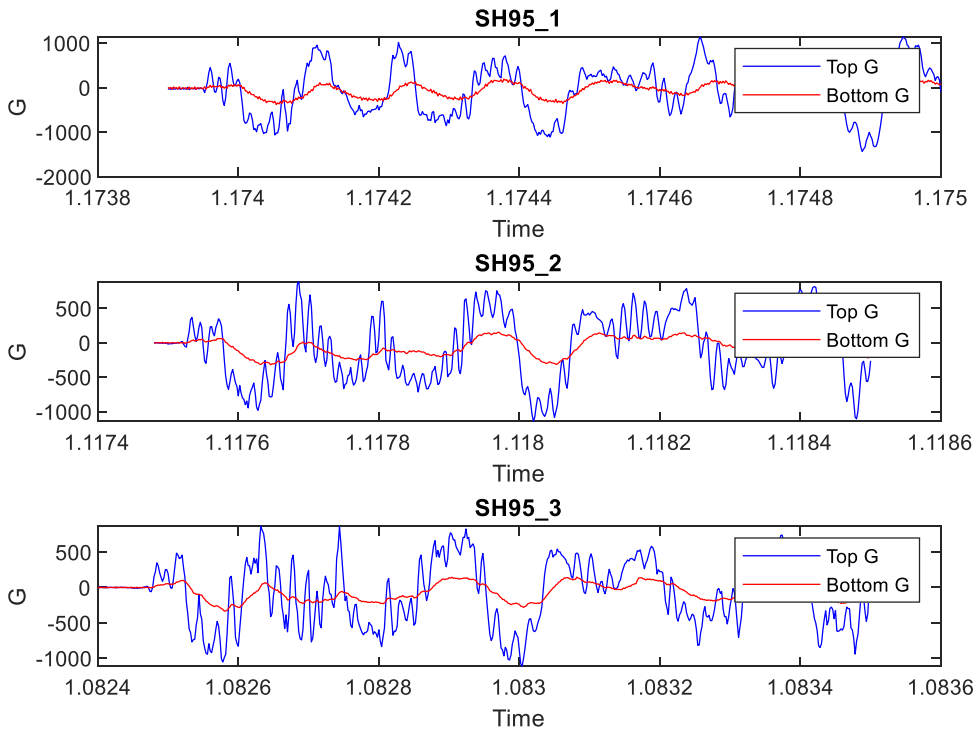
Figure 28:The acceleration reduction of the hybrid material SH95 specimens at the moment of the impact under the drop tower at 2 m/s
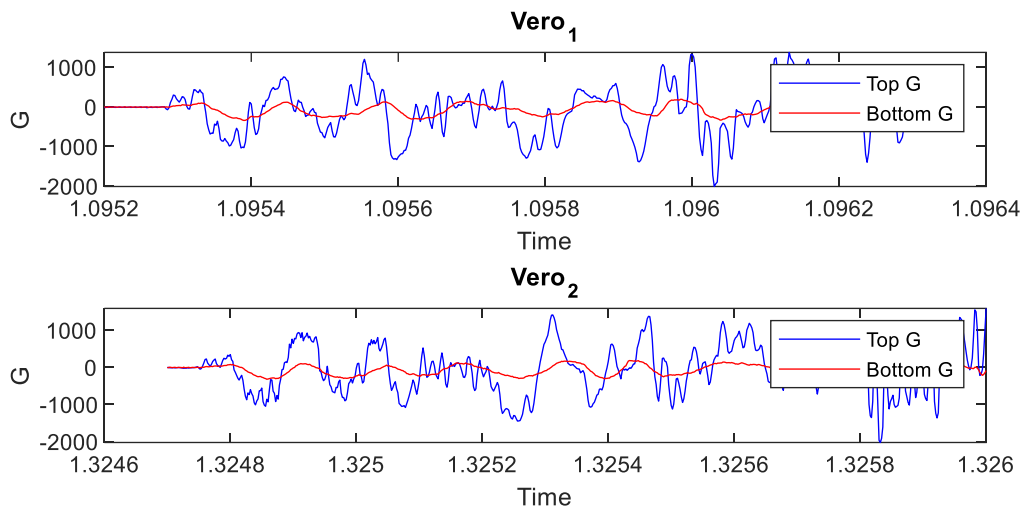
Figure 29:The acceleration reduction of the Vero specimens at the moment of the impact under the drop tower at 2 m/s
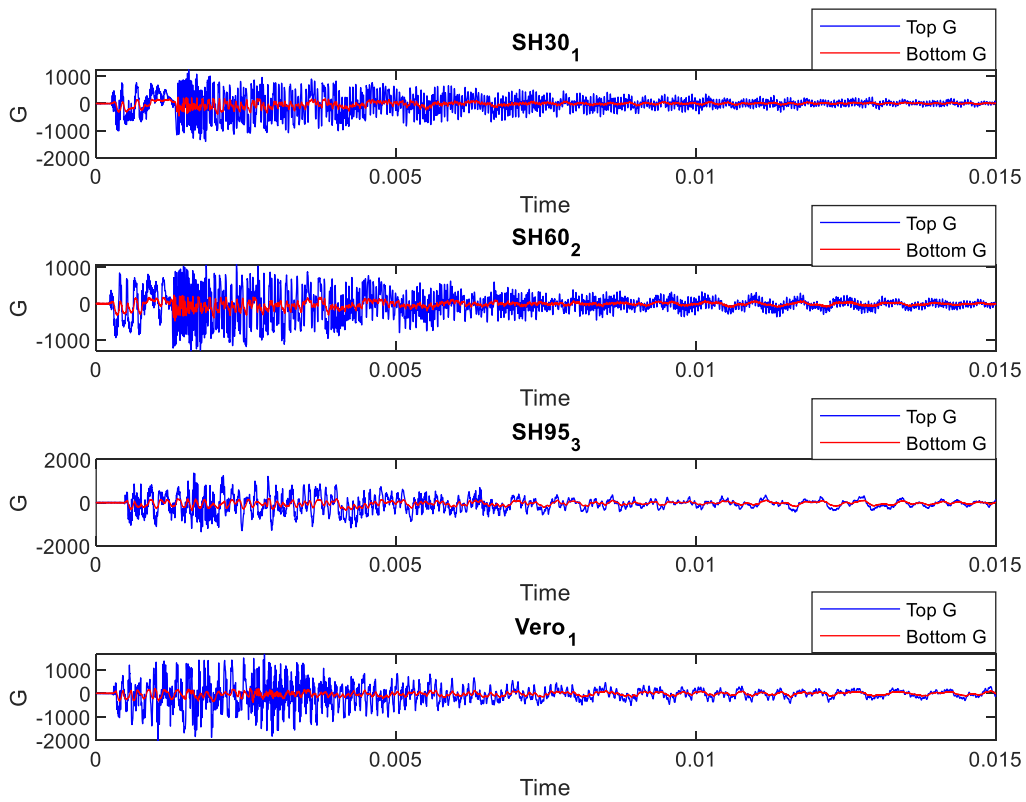
Figure 30:An acceleration reduction comparison between the four tested materials of the first 0.0.15 seconds after the impact

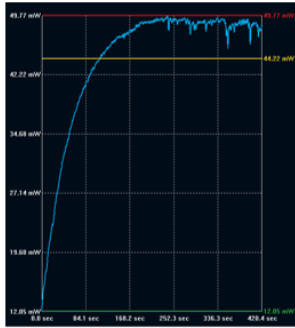**0.25 mm Thickness [Laser power meter readings]**
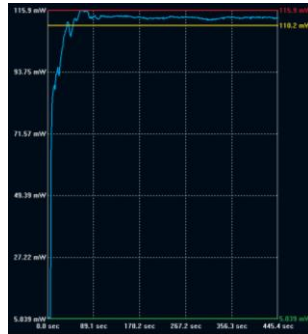
fig: test 1   fig: test 2   fig: test 3

Figure 31: Laser power meter readings of 0.25 mm thickness Agilus30 samples.

0.5 mm Thickness [Laser power meter readings]
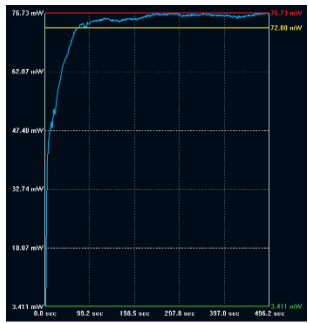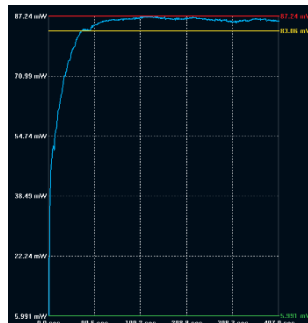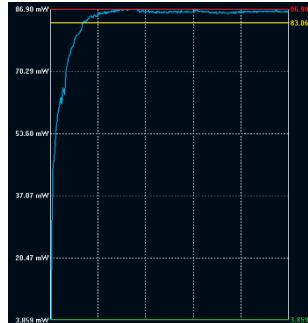
fig: fig: test   fig: test 3

Figure 32: Laser power meter readings of 0.50 mm thickness Agilus30 samples.

1 mm Thickness [Laser power meter readings]
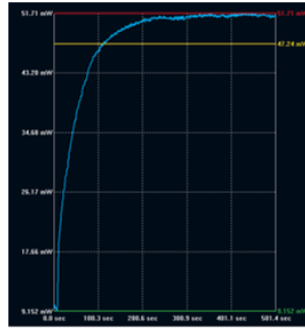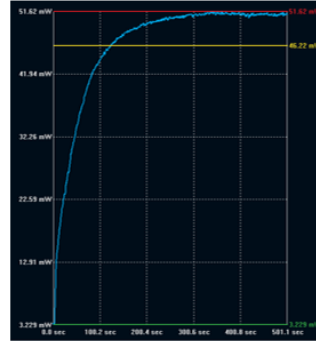

fig: test 1   fig: test 2   fig: test 3

Figure 33: Laser power meter readings of 1 mm thickness Agilus30 samples.
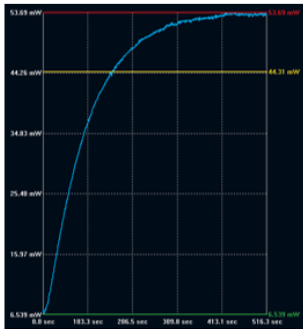
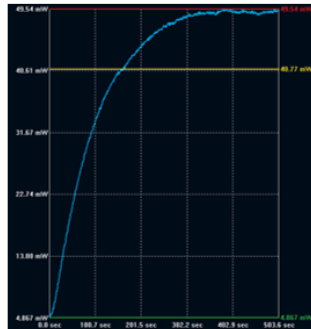**2 mm Thickness [Laser power meter readings]**
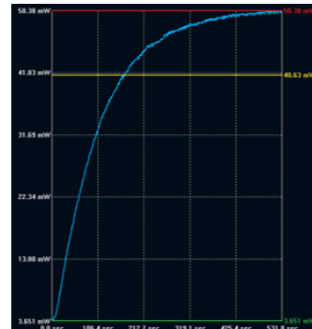

fig: test 1   fig: test 2   fig: test 3

Figure 34: Laser power meter readings of 2 mm thickness Agilus30 samples.